DESTRESS

Demonstration of soft stimulation treatments
of geothermal reservoirs

Deliverable 6.1: Soft chemical/acid stimulation

Best practice workflows and tools

WP 6: Intelligent tools controlling performance and environment

Lead Beneficiary	TNO
Type	☑ R - report, document etc. ☐ OTHER - software, technical diagram etc. ☐ DEM - demonstrator, pilot etc. ☐ E - ethics ☐ DEC - website, patent filing et++c.
Status	☑ Draft ☑ WP manager accepted ☑ Project coordinator accepted
Dissemination level	☑ PU - Public ☐ CO - Confidential: only for members of the consortium
Contributors	☑ 1-GFZ ☐ 5-GES ☐ 9-GTL ☐ 13-SNU ☐ 2-ENB ☑ 6-TNO ☐ 10-UoS ☐ 14-KIC ☐ 3-ESG ☑ 7-ETH ☐ 11-TUD ☐ 15-ECW ☑ 4-UoG ☐ 8-GTN ☐ 12-NEX ☐ 16-WES
Creation date	29-10-2019
Last change	27-02-2020
Version	4
Due date	29.02.2020
Submission date	28.09.2020

This project has received funding from the European Union's
Horizon 2020 research and innovation programme
under grant agreement No 691728

Summary

The scope of task 6.1 is to predict the performance of chemical treatments as dependent on rock petrology, fluid geochemistry and reservoir conditions. In the view of soft-stimulation of geothermal reservoirs, alternatives to harsh acid stimulation are explored for more soft chemical treatment.

The success of acid stimulation could be simply linked to the potential of a rock to dissolve and the resulting improvement of flow properties. However acid stimulation is notorious for its unreliability, indicating that the process is more complex. To optimize the performance of acid injection and prevent failures, it is recommended to follow a workflow including rock sampling, sample analyses, laboratory experiments, predictive numerical modelling and uncertainty assessment. The work performed in task 6.1 covers different elements of this workflow and contributes to a better insight in the factors controlling chemical treatment for enhancing reservoir permeability. Furthermore, the work helps selecting the best suited tools to assess the effectivity of chemical stimulation.

This deliverable contains a synthesis of the studied workflow components. The technical work performed by the different partners is collected in three appendices:

Appendix A: Characterisation of analogue and core samples (UoG)

The work was focussed on analysing core and analogue outcrop samples for a better understanding of the poor flow properties of the Klaipeda geothermal plant. The aim was to use X-Ray computed tomography (X-CT) analysis to determine the fluid flow properties (porosity) and the presence of pervasive clay fines or carbonate cementation blocking pore space within the sandstone samples. Core samples from the Klaipeda site were used as well as Devonian sandstones that provide the closest analogues to the rocks of the Klaipeda geothermal reservoir. The X-CT results show a low porosity of the Klaipeda reservoir rocks and significant carbonate cementation that can explain the low geothermal performance. There were significant differences in cementation between the outcrop and core samples and hence caution is recommended when using outcrop samples for pre-drill porosity predictions of a geothermal reservoir.

Appendix B: Experimental procedures for sample characterisation (ETH)

Different sample analysis techniques (including Mercury intrusion porosimetry, scanning electron microscope and Micro-computed tomography) were performed in order to optimize the assessment of rock properties and provide input for predictions of stimulation potential. The conducted measurements successfully characterize the hydraulic and chemical properties of a sandstone sample from the borehole Vydmantai-1. The sandstone has a high porosity of 21.9% and a relatively high permeability of 356 mD. The sandstone contains 12 vol.% dolomite cement, which is recognized as the most reactive mineral in this sandstone. About 40% of the dolomite surface area is exposed to pore space, indicating a high potential for dissolution during acid stimulation.

Appendix C: Numerical predictions of chemical treatment in geothermal reservoirs (TNO)

Numerical simulations were performed of acid injection and water flow during geothermal exploitation with the aim of predicting the effectiveness of chemical treatment. Thermo-hydraulic-mechanical-chemical (THMC) modelling is used to investigate the coupled processes during acid stimulation. Reactive transport modelling (RTM) is applied to study soft-acidizing with CO_2 alternatives for acid stimulation such as. Acid stimulation with HCl is effective in dissolving carbonate (cement) in sandstones. However, the dissolution potential of cold water can achieve the same results. When the geothermal fluid is CO2 enriched, the soft-stimulation potential of the geothermal fluid is even larger and results in an increased area of carbonate dissolution around the wellbore.

Workflows and tools to define the effectiveness of soft chemical/acid stimulation

1. Introduction to injectivity issues and chemical treatment

A key challenge in geothermal energy production is a disappointing permeability or a decline of injectivity over time (Schreiber et al., 2016). Blockage of the reservoir pore space, induced by the geothermal operations, reduces the permeability and hence the injectivity of the reservoir (Ungemach, 2003, Blöcher et al., 2016, Gallup, 2009). In the case of insufficient injectivity of the targeted geothermal formation, the reservoir rock can be stimulated, as is common practice in the oil and gas industry since the 1960s (Ali et al., 2016, Portier et al., 2007, Rea and Di Lullo, 2003). Most practiced stimulation methods involve acid injection or hydraulic fracking. Acid stimulation can be applied to dissolve materials causing flow obstruction such as primary cementation, drilling damage, reservoir scaling and particle clogging. Different materials can be responsible for clogging the pores, including reservoir fines, bacteria, corrosion products, scale particles or in situ precipitating minerals induced by chemical interaction between the injected brine and reservoir (Ungemach, 2003, Boch et al, 2017).

The research activities reported in this deliverable focussed on geothermal reservoirs with primary permeability in (carbonate cement containing) porous sandstones, i.e. not fracture dominated. The type of acid stimulation applicable to this rock type would be matrix acidizing. This means dissolution of certain minerals in the rock (in the matrix) by acid injection at a pressure below the formation fracturing pressure (Ali et al., 2016, Portier et al., 2007). Although frequently applied, there are still major challenges in successful acid stimulation of a reservoir related to: uncertainty in the type(s) of formation damage, uncertain in the mineralogy of the rock, adverse chemical reactions between acid and rock minerals, inadequate coverage and limited acid penetration, and rock deconsolidation due to mineral dissolution (Portier et al., 2007). These challenges may cause an acid job to fail due to an incorrect acid design (rate, volume), poor acid selection, use of inappropriate acid additives, insufficient iron control or improper acid placement (Rea and Di Lullo, 2003). After decades of application, there is still a failure rate of acid jobs of 32 % in the oil and gas industry (Portier et al., 2007).

A number of acid types can be used for acid stimulation (Ali et al., 2016, Portier et al., 2007, Rea and Di Lullo, 2003). The most common are: hydrochloric (HCl), hydrofluoric (HF), acetic (CH_3COOH), formic (HCOOH), sulfamic (H_2NSO_3H) and chloroacetic ($ClCH_2COOH$). The most popular acid used for matrix stimulation of sandstones is a combination of HF and HCl, which is known as ‘mud acid’ in the oil and gas industry. The trend in mud acid concentration is towards higher HCl concentrations, with the previous standard of concentration 3% HF + 12% HCl and 1.5% HF + 13.5% HCl becoming more common (Portier et al., 2007). HF is required to dissolve silicate minerals but there is also a risk of precipitating reaction products due to chemical interaction of HF and aluminosilicates. There are three classes of HF reactions: primary, secondary and tertiary (Ali et al., 2016). Primary reactions are related to the presence of calcium (Ca^{2+}) which combines with HF to form calcium fluoride (CaF_2). Sodium (Na^+) and potassium (K^+) can create alkali-fluosilicates and alkali-fluoaluminates when Na^+ or K^+ in the brine react with HF. Secondary reactions are driven by the greater affinity of fluorine for aluminum than for silicon, which can cause the precipitation of silicium or aluminum complexes. To prevent these reactions HCl is added to HF, since HCl can keep the pH low and prevents the formation of fluorosilicates, fluoroaluminates, and fluoride salts. Tertiary reactions are the reactions of the aluminum fluorides and aluminosilicates but these reactions are not significant at temperatures below 90°C.

Acid stimulation can be costly and insufficient or even counterproductive when reaction products clog the pore space. Geothermal operators would greatly benefit from more low-cost, environmentally friendly and soft-stimulating strategies for chemical treatment of geothermal reservoirs. Soft-acidizing

with CO_2 could be an effective alternative to improve the flow properties of a reservoir (Wasch et al., 2020). Adding dissolved CO_2 to the injection water will reduce the pH which causes dissolution of carbonate minerals when present in the reservoir. Variable dissolved CO_2 concentrations can be found in the subsurface and many doublets show gas release from the produced water due to the pressure decrease and corresponding gas solubility decrease. This is especially true for Dutch geothermal reservoirs which deal with a relatively high CO_2 partial pressure (Wasch 2014). Since CO_2 is naturally present there is a low probability of adverse reaction precipitates, which can form during acid injection (Ali et al., 2016, Portier et al., 2007). Re-injecting the CO_2 from the produced geothermal water, or even maximizing CO_2 co-injection in the injected water, could stimulate the injectivity of (low permeable) formations and support CO_2 emission reductions at the same time, improving the sustainability of geothermal energy. Similar to acid injection, soft-stimulation by CO_2 re- or co-injection has a risk of rock deconsolidation due to mineral dissolution (Portier et al., 2007). This risk needs to be investigated with coupled geochemical and geomechanical models and laboratory experiments.

2. Objective

The objective of Task 6.1 of the Destress project was to develop a workflow and methodology recommendations for the assessment of initial or production-related low permeabilities in geothermal reservoirs and for the evaluation of chemical treatment techniques. The development of this methodology was foreseen to be supported by samples and data from acid stimulation field tests from selected pilot sites in Europe. The field tests could not be performed and studied during the Destress project for various reasons, hampering the execution of the full workflow. For this reason, several elements of the workflow have been tested on different sites and samples, with the numerical modelling being a theoretical exercise.

This deliverable reports on:

- Concept workflow and recommended tools (Chapter 3)
- Analyses of core and analogue outcrop samples for a better understanding of the poor flow properties of the Klaipeda geothermal plant (Appendix A)
- Sample analysis techniques with the aim of optimizing the assessment of rock properties such as pore space and reactivity (Appendix B)
- The development of reactive transport models (RTM) and coupled Thermo-hydraulic-mechanical-chemical (THMC) models for assessing and predicting the performance of chemical treatment techniques (Appendix C)

3. Concept workflow and tools

Proper design of an acid stimulation – such as type, volume and rate of acid injection – requires a systematic workflow (Peksa et al., 2016). To optimize the performance of acid stimulation and prevent failures, it is recommended to follow a workflow that includes rock sampling, sample analyses, laboratory experiments, predictive modelling and uncertainty assessment (Figure 1). By applying and optimizing this workflow we aim to provide methodology and tool recommendations for assessing the performance of chemical treatment.

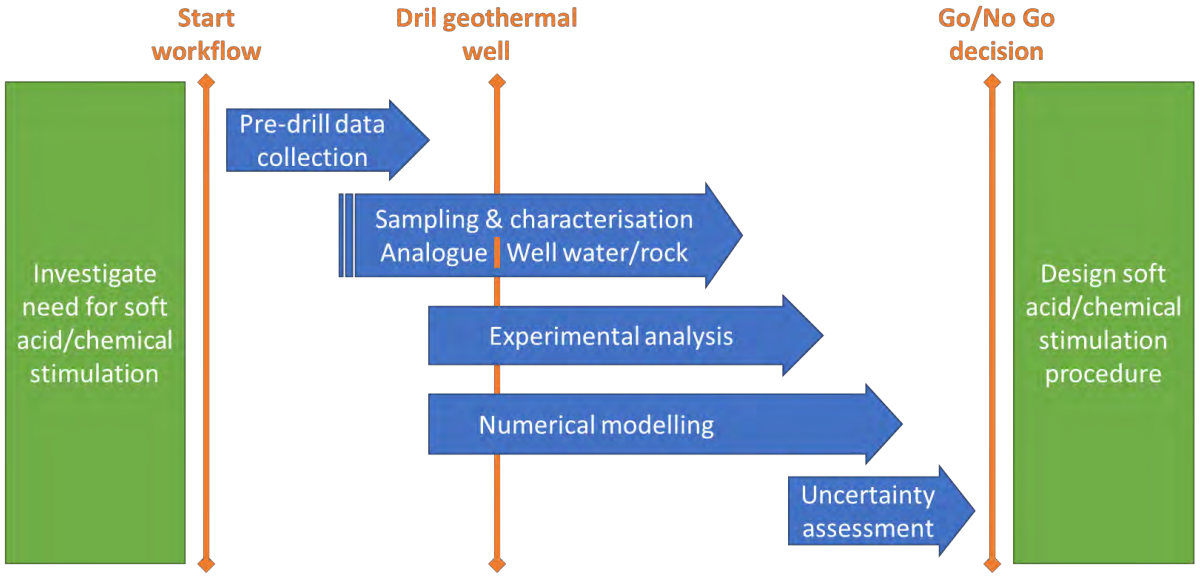

Figure 1. Gantt flowchart to predict and advise on soft chemical/acid stimulation

3.1 Pre-drill data collection

A successful acid job requires detailed information on the (near-well) reservoir mineralogy, the brine fluid composition and the accessibility of minerals to the pore space and hence the acid. In the pre-drill stage, this data can be obtained from neighbouring wells penetrating the same reservoir, or from outcrop analogues. Although these samples may provide valuable insights in the expected mineralogy, caution is advised regarding lateral facies differences or differences in burial history. The latter is especially true for outcrop analogues; comparison of core samples from the Klaipeda geothermal site and Devonian sandstones showed significant differences in cementation and resulting flow properties (Appendix A).

3.2 Sample characterisation for acid performance prediction

Strongly depending on the mineralogy and primarily the spatial distribution of carbonate and sulphate minerals, the results of chemical stimulation using acid injection into sandstones are challenging to be predicted. On the one hand, the injected acid solution dissolves solids (e.g. carbonates) and potentially enlarges the pore space; on the other hand, these dissolution reactions could induce rock weakening and/or release of fine particles , resulting in rock compaction and/or flow path clogging, respectively. These mechanisms can lead to adverse effects on the rock permeability (i.e. reservoir injectivity/productivity). It is recommended to first examine the rock mineralogy and mineral/pore distribution by SEM imaging, and then to perform in situ reactive flow-through experiments on the rock samples (Appendix B). Results from these flow-through experiments can give an indication of the potential permeability alteration upon acid stimulation. Moreover, analyses of SEM images often provide important information, such as mineral volume percentage, mineral reactive surface area, pore size distribution, etc., to further support the interpretation of the experimental observations.

3.3 Numerical tools

Predictive modelling enables pinpointing the most likely causes of failing reservoir flow, as well as the possibilities for flow improvement. Modelling a variety of scenarios or stochastic modelling is a powerful tool for uncertainty assessment and feasibility studies since many options for chemical stimulation can be tested and various conditions can be applied.

Reactive transport modelling is ideally suited for predictions of acid reactivity and potential changes in flow properties related to mineral reactions (Appendix C). It should be noted that reactive transport modelling is useful for simulating dissolution and precipitation reactions, whereas processes such as fines migration are not included. Model results showed that performance enhancement by soft-stimulation is complex due to the interplay of fluid density, injected mass and pore volume changes (Appendix C). Acid stimulation with HCl is effective in dissolving carbonate (cement) in sandstones, however, the dissolution potential of the cold and unacidified injection water can also result in carbonate dissolution due to the higher solubility of carbonates at lower temperatures. When the geothermal fluid is enriched in CO_2, the soft-stimulation potential of the geothermal fluid increases and results in a larger area of carbonate dissolution around the wellbore.

Thermo-hydro-mechanical-chemical (THMC) models have great potential to incorporate the mechanical response of the reservoir (Appendix C). This could include the formation of cold water fracs, which would increase the permeability of a rock and enhance performance. However, there could also be changes in stress due to pore volume enhancement by chemical treatment. The degradation of the rock material by carbonate dissolution could lead to pore collapse which is detrimental to the flow properties. A THMC model has been developed in this project for a first study of coupled processes. However detailed input is required on the change in material properties, derived from laboratory experiments (Appendix B).

REFERENCES

1. Ali S.A., Kalfayan L., and Montgomery C., *Acid stimulation*, SPE Monograph Series, Vol. 26, 305 pp, 2016.
2. Blöcher, G., Reinsch, T., Henninges, J., Milsch, H., Regenspurg, S., Kummerow, J., and Huenges, E.: Hydraulic history and current state of the deep geothermal reservoir Groß Schönebeck, Geothermics, 63, (2016), 27-43.
3. Boch, R., Leis, A., Haslinger, E., Goldbrunner, J. E., Mittermayr, F., Fröschl, H., and Dietzel, M.: Scale-fragment formation impairing geothermal energy production: interacting H_2S corrosion and $CaCO_3$ crystal growth, Geothermal Energy, 5(1), (2017), art. no. 4.
4. Gallup, D.L.: Production engineering in geothermal technology: A review, Geothermics, 38(3), (2009), 326-334.
5. Huq, F., Haderlein, S.B., Cirpka, O.A., Nowak, M., Blum, P., Grathwohl, P. (2015) Flow-through experiments on water–rock interactions in a sandstone caused by CO_2 injection at pressures and temperatures mimicking reservoir conditions, Applied Geochemistry, 58, 136-146.
6. Peksa A., Naveen Ilangovan, Fiorenza Deon, Hamidreza M. Nick, David Bruhn, A workflow for laboratory and numerical analysis of matrix acidizing in geothermal wells, Kennisagenda Aardwarmte: Soft stimulation techniques - D1, 2016.
7. Portier, S., L. André, and F.-D. Vuataz, Review on chemical stimulation techniques in oil industry and applications to geothermal systems. Engine, work package, 2007. 4: p. 32
8. Rae, P., & Di Lullo, G. (2003, January 1). Matrix Acid Stimulation - A Review of the State-Of-The-Art. Society of Petroleum Engineers. doi:10.2118/82260-MS
9. Schreiber, S., Lapanje, A., Ramsak, P., and Breembroek, G.: Operational issues in geothermal energy in Europe: Status and overview (2016).
10. Ungemach, P.: Reinjection of cooled geothermal brines into sandstone reservoirs, Geothermics, 32(4-6), (2003), 743-761.
11. Wasch, L.J.: Geothermal Energy-Scaling potential with cooling and CO_2 degassing. TNO report. TNO 2013 R11661. (2014).
12. Wasch, L.J., Dijkstra, H.E. and Koenen, M.K., Soft-stimulating Injection Procedures to Improve Geothermal Reservoir Performance - Proceedings, World Geothermal Congress, 2020 Reykjavik.

Appendix A Characterisation of analogue and core samples

Sean Watson, Rob Westaway, Neil Burnside, Nicolas Beaudoin

University of Glasgow

The objective of this work was to assess the fluid flow properties and the presence of clay fines or cementation within Devonian sandstones that provide the closest possible analogues to those forming the Klaipeda geothermal reservoir. Field and borehole core samples were obtained from sites in Lithuania and Latvia, including the Klaipeda 1I well. Using X-Ray computed tomography and image processing techniques, the porosity of each sample was determined.

This chapter describes a methodology to evaluate sample porosity as input for predictive modelling on clogging potential and chemical treatment procedures.

1. Geological Overview

Lithuania contains a varied geological sequence comprising of a largely continental sedimentary sequence which dips and thickens towards the north-west, overlying metamorphic and metasedimentary basement rocks of the Pre-Cambrian Baltic Shield (Brehme et al., 2019). Potential geothermal resources have been identified in three stratigraphic horizons in Lithuania: (i) the Upper-Middle Devonian Šventoji (D_3) – Upninkai (D_2) complex; (ii) the Middle – Lower Devonian Parnu-Kemeri-Gargždai (D_2-D_3) complex; and (iii) Cambrian Deimena – Kybartai – Gegè – Virbalis strata (Brehme et al., 2019). The Upper Devonian (D_3-D_2) complex comprises the Šventoji and Upninkai Formations which are composed of sands and poorly cemented sandstones, silts, clays and some dolomitic marls (Brehme et al., 2019). The Middle to Lower Devonian Kemeri Formation comprises friable sandstones with interlayers of strongly cemented sandstones. These interlayers are cemented by clay, carbonates, gypsum and quartz, with siltstone and shale interlayers (Zinevicius et al., 2020). The rocks that form the geothermal reservoir at Klaipeda are designated the Viešvile Formation of Early Devonian age. The Viešvile Formation is a sub-unit within the Kemeri Formation. The westward thickening sedimentary sequence is illustrated in Figure A1. The Devonian age formations present in the subsurface at Klaipeda become progressively shallower moving eastwards across Lithuania.

At the time when the Devonian reservoir rocks were deposited, Lithuania was located at subtropical latitudes in the southern hemisphere near the SE margin of the ancient continent of Laurussia. As a result of earlier motions of tectonic plates, Laurussia was transected by the Caledonian mountain range, erosion of which provided the source of the widespread sandy sediments deposited at this time. The Earth's climate at the time is not yet fully understood, but it is thought (e.g., Kiipli et al., 2016) that along the SE margin of Laurussia aridity was interspersed with moisture as a result of monsoon systems originating in the ocean located to the southeast. Rocks in the Baltic region, dating from this time, thus consist not only of sandstone; the product of erosion of the Caledonian mountains; but also, abundant clay minerals; the product of chemical weathering of rocks; indicating a subtropical environment (e.g., Kiipli et al., 2016).

There is a possibility therefore that the blockage of flow in the Klaipeda geothermal project might be a consequence of pervasive clay minerals blocking pore space within the sandstone. On the other hand, it is possible that the cause relates to chemical precipitation as a result of changes in the temperature and pressure in the circulating fluid. Conceivably a combination of mechanisms, including these, might be in operation. Another potential mechanism for making the Viešvile Formation sandstone beneath

Klaipeda relatively impermeable is the presence of calcium carbonate cement between sand grains (Pipira et al., 2015). Such cementation might be expected as a result of evaporation of groundwater shortly after deposition, thus indicating warmth and aridity in the palaeoclimate.

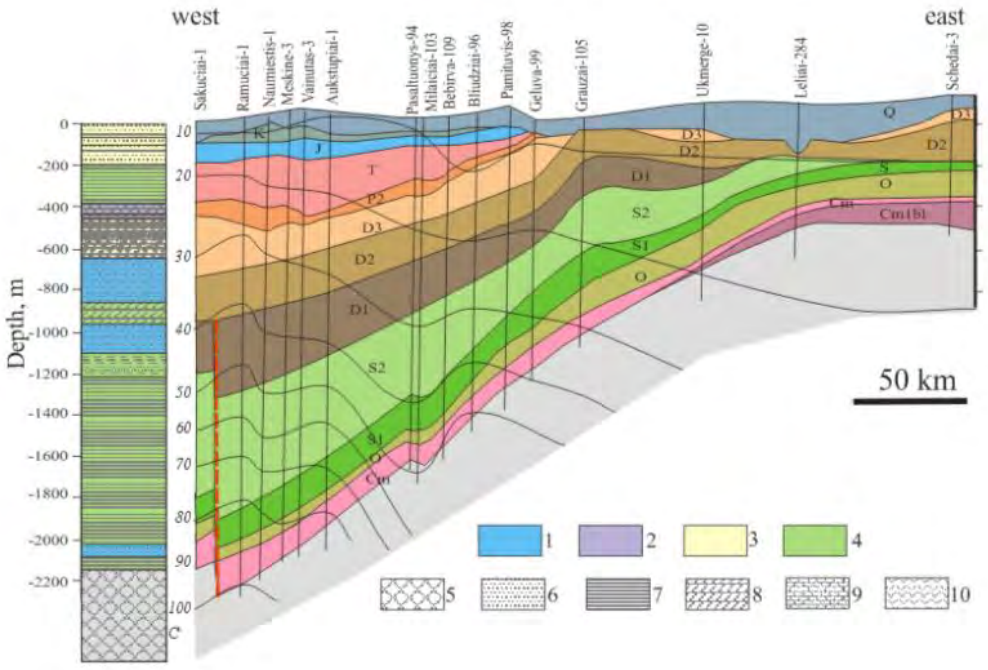

Figure A1: Geological cross-section oriented west-east across Lithuania, from Zinevicius et al., (2015). Lithological profiles are indicated on the left. 1 – major aquifer, 2 – subordinate aquifer, 3 – intercalations of aquifers and aquitards, 4 – aquitard, 5 – crystalline basement, 6 – sandstone, 7 – clay/shale, 8 – marlstone, 9 – carbonates, 10 – gypsum.

2. Fieldwork

As a result of a literature review, dialogue with local specialists and consultation of large-scale geological maps of the area, the localities where the reservoir rocks (indicated in Figure A1) outcrop were identified. In April 2017, fieldwork was conducted to visit these localities in Lithuania and Latvia to collect samples from the Devonian sandstone outcrops. In Latvia these are locally named the Amata Formation and the Burtnieki Formation (Figure A2). Deposits of the Burtnieki Formation were studied at the Veczemji Cliffs in Latvia (35 N 42662 85349) where clayey siltstones and sandstones are exposed in an outcrop by the Gulf of Riga. Deposits of the Amata Formation were studied at outcrops at the Erglu and Zhiguli Cliffs and at the Amata River.

In addition, borehole core samples of the Viešvile Formation were obtained from the Vievis Core Archive near Vilnius, Lithuania, from the following boreholes: Klaipeda-1I, Palanga-318a and Vydmantai-1. The Vydmantai-1 and Palanga-318a wells are located around 30 km north of the Klaipeda geothermal site and due to the low lithological and petrophysical lateral variability of the sandstone reservoir, are considered analogous with the Viešvile Formation encountered at Klaipeda. Both of these boreholes encountered strata which consist of fine-grained sandstone, dolomite, clay and gypsum.

Nineteen samples of borehole cores were collected and 13 samples from outcrop sites. A number of the outcrop samples were poorly consolidated and due to their fragility, were deemed unsuitable for sample preparation and analysis. From the remaining suite of samples, a selection of the most representative were chosen for X-CT analysis. These samples are shown in Table A1 and Table A2.

Figure A2: Outcrop of Amata Formation, Latvia. (UTM Grid Ref: 35 N 69431 38869).

Table A1: Core Samples

Name	Formation	Borehole	Depth (m)
KLA 1I	Viešvile Formation	Klaipeda 1I	1107.4
PAL 918	Viešvile Formation	Palanga 318a	918
PAL 937	Viešvile Formation	Palanga 318a	937
VYD 984	Viešvile Formation	Vydmantia 1	984
VYD 987.6	Viešvile Formation	Vydmantia 1	987.6

Table A2: Outcrop Samples

Name	Formation	UTM Coordinates	Location
A1	Amata Formation	35 N 87640 48009	Amata River
E1	Amata Formation	35 N 95422 58937	Erglu Cliffs on the Gauja River
V1	Burtnieki Formation	35 N 42662 85349	Veczemji Cliffs, Tūja
Z1	Amata Formation	35 N 92750 43793	Zhiguli Cliffs on the Amata River

3. X-CT Methodology

X-Ray computed tomography (X-CT) is a non-destructive and non-invasive method which uses contrasts of X-ray attenuation (a function of density and atomic number) to reconstruct the 3D distribution of areas of different densities within a large variety of materials. The 3D reconstruction is based on a series of contiguous 2D radiographs taken with different view angles, by rotation a sample around a single axis in small steps. X-CT has been increasingly used in earth sciences over the past two decades (Ketcham and Carlson, 2001; Cnuddle and Boone, 2013). Amongst many other examples, X-CT analysis has been successfully utilised to unravel the shape, orientation and 3D distribution of minerals, porosity and cracks in sedimentary rocks (e.g. Noiriel, 2015).

The X-CT scans were performed using a Nikon XTH 320/225 system at the Advanced Materials Research Laboratory at Strathclyde University. This facility is funded by the Scottish Government Oil and Gas Innovation Centre (OGIC) and shared between University of Glasgow and Strathclyde University. The Nikon XTH 320/225 system is equipped with a 225-kV reflection gun and a 2000 * 2000-pixel flat panel photodetector (cell size 0.2 x 0.2 mm). No filters were used for the scans.

The first sample to be scanned was KLA 1I. This sample was scanned in its original state given the need to preserve core material from this borehole. Given the size of the core sample the scanned voxel size (resolution) was 31.66 µm. The exposure time for each projection was 708 ms lasting for 1600 projections.

For the remainder of the scanned samples it was possible to prepare a small chip of the core or outcrop material. This allowed for an improved scan resolution and the smaller pores to be observed. For these samples, the exposure time for each projection was 2829 ms, lasting for 1600 projections. The X-Ray source to sample distance was set to achieve an approximate minimal voxel size of 3.5-5 µm. The accelerating voltage and current of the X-Ray varied depending on the target voxel size. Scanning conditions are summarised in Tables A3 and A4.

Table A3: X-CT Operational Details for Borehole Samples

Name	Resolution (µm)	Scan Size (µm)	X-Ray (kV)	X-Ray (µA)
KLA 1I	31.66	-	170	28
PAL 918	3.50	4109.27 x 2881.73 x 5441.72	145	21
PAL 937	3.50	4343.58 x 4493.97 x 5403.25	145	21
VYD 984	3.50	3210.48 x 3934.41 x 5452.21	145	21
VYD 987.6	3.50	2748.84 x 4347.08 x 5329.81	145	21

Table A4: X-CT Operational Details for Outcrop Samples

Name	Resolution (µm)	Scan Size (µm)	X-Ray (kV)	X-Ray (µA)
A1	4.50	2755 x 3502.27 x 2358.85	159	25
E1	5.00	6999 x 5499.92 x 6999.9	110	41
V1	4.50	5401.91 x 6752.39 x 6752.39	159	25
Z1	5.00	4219.97 x 5464.97 x 5759.97	110	41

To ensure accurate quantitative results it is necessary to have high quality images that avoid sources of error, such as artefacts due to the reconstruction process. 3D volumes were reconstructed from projections using the CT Pro 3D software (© 2004-2016 Nikon Metrology), with an automatic reconstruction tool to find the scan's centre of rotation and applying a beam hardening correction (Brooks and Dichiro, 1976). Ring artefacts, which are common in micro X-CT, did affect the segmentation process however this was mitigated by removing the slices affected. All volumes were reconstructed in 16 bits (65536 grey values).

To reconstruct the surfaces of the samples, the 3D volumes were processed using Avizo (v.9.2.0, © FEI), for the KLA 1I sample, and Dragonfly (v. 4.1.0.647, © Object Research System (ORS) Inc.), for the remainder of the samples. The following image processing analysis was performed in both software packages.

First, the noise was reduced by applying an edge-preserving smoothing filter (''bilateral filter") that averages the intensity value of a voxel with regard to the intensity value of its neighbours, considering a number of neighbours defined by a 3 x 3 x 3 kernel size. To reduce the effect of ring artefacts and beam hardening at the edges of the sample, a sub-volume within the sample was created using the "crop" tool. This allowed mitigation of the aforementioned affects as well as limiting the opportunity to segment external air, and instead only focusing on the internal pore space. Each phase (mineral and pore) were separated manually using simple greyscale thresholding, by segmentation of the volumes corresponding to the relative density range of each individual phase. Segmentation is considered as optimal when the selected range of grey values selects all the voxels belonging to the pore phase while it does not select voxels that belong to the mineral phase. Such optimal separation is achieved due to a strong contrast between the phases. Pixels attributed to noise were then removed using the "remove small spot" function, which consists of deleting all clusters of less than 10 pixels from the segmented 3D data. The volume of the mineral phase and the volume of the pore phases were then determined by the software packages by "counting" the voxels in the respective voxel clusters. The choice of grey scale value used to segment the pores and the minerals phases has an influence on the resulting value of porosity within the sample volume. In order to achieve the optimal value, a sensitivity analysis was conducted to determine the porosity using numerous grey scale values used to represent the segmented pore space.

4. X-CT Results

This section details the results of the X-CT analysis of the borehole and outcrop samples. As previously described, for each sample, a range of porosity is given based upon the segmentation sensitivity analysis (Table A5). A value of porosity adjudged to be the most representative of the sample scan is shown. Furthermore, example output of the X-CT scans is shown, post image processing (Figure A3). The range of greyscale values indicates pores, grains and cementation.

Table A5: X-CT Porosity Results

Name	Formation	Depth (m)	Porosity (%)	Porosity Range (%)
KLA 1I	Viešvile Formation	1107.4	8.40	-
PAL 918	Viešvile Formation	918	18.05	16.94-20.33
PAL 937	Viešvile Formation	937	22.23	19.52-24.58
VYD 984	Viešvile Formation	984	9.60	5.96-14.77
VYD 987.6	Viešvile Formation	987.6	3.11	2.55-3.83
A1	Amata Formation	Outcrop	25.34	21.06-28.66
E1	Amata Formation	Outcrop	23.38	22.01-24.77
V1	Burntieki Formation	Outcrop	28.01	14.44-36.03
Z1	Amata Formation	Outcrop	7.93	5.88-10.43

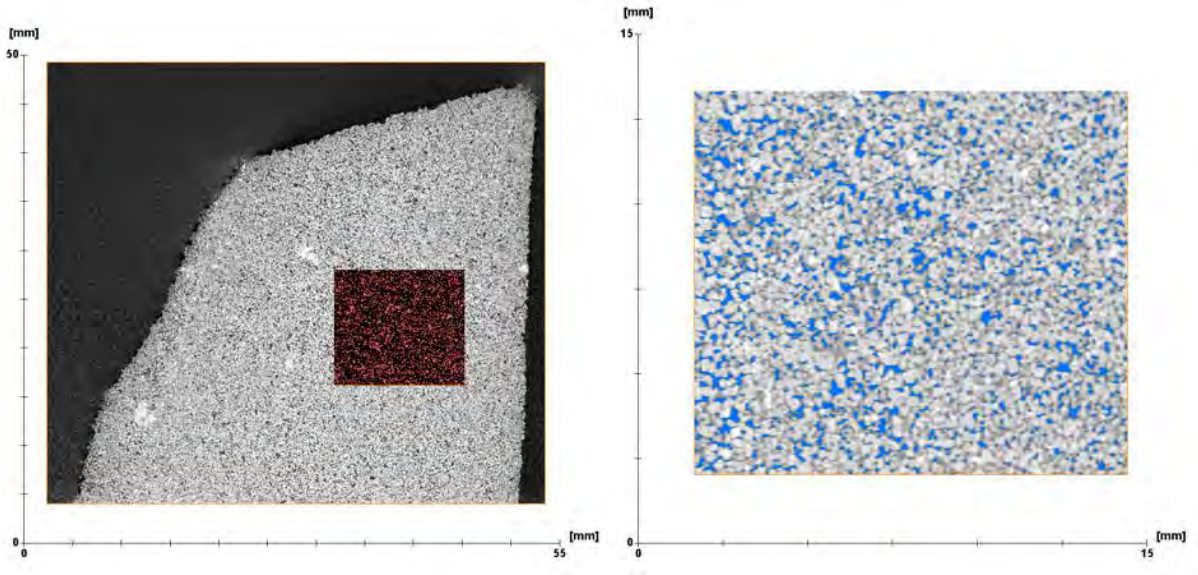

Figure A3: Left: Ortho-slice of KLA-1I in greyscale with extracted sub-volume area shown. Right: Ortho-slice of sub-volume of KLA-1I in greyscale with thresholded pores shown in blue.

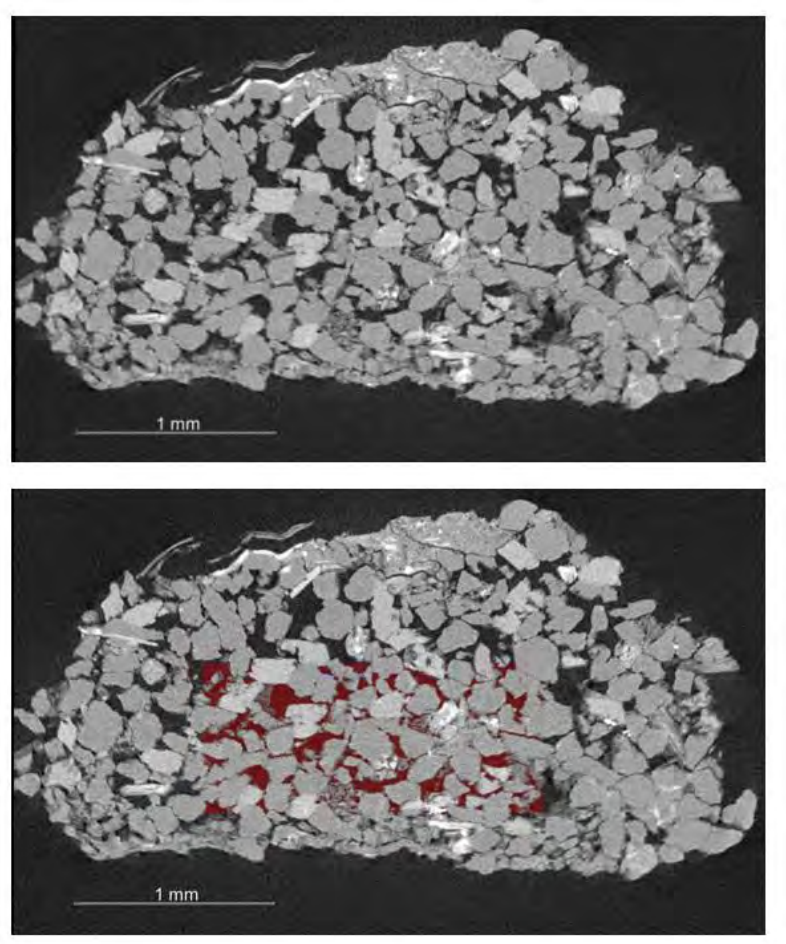

Figure A4: Top: XY view of PAL 918 sample in greyscale. Bottom: XY view of PAL 918 sample in greyscale with thresholding of pores in sub-volume area shown in red.

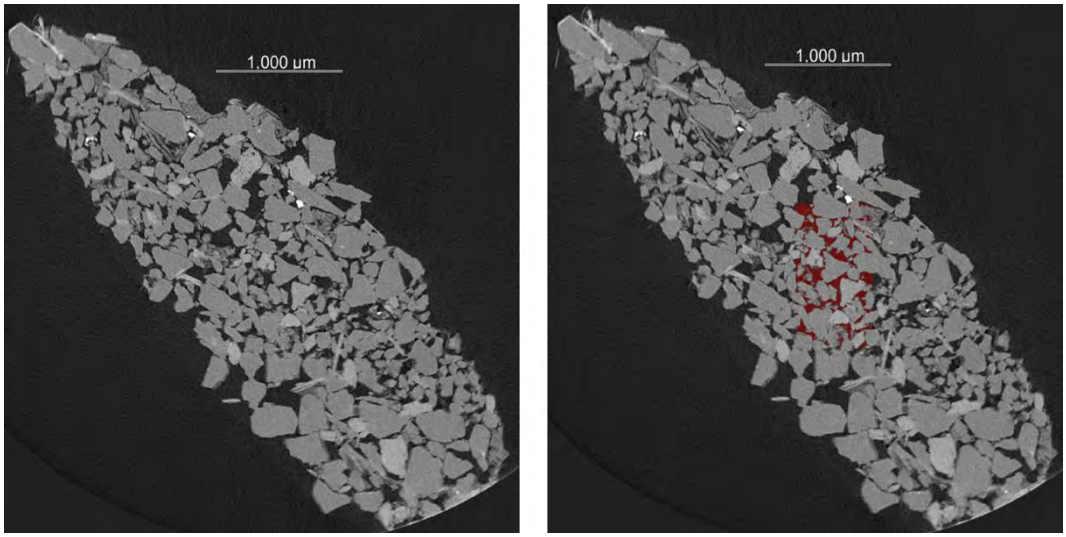

Figure A5: Left: XY view of PAL 937 sample in greyscale. Right: XY view of PAL 937sample in greyscale with thresholding of pores in sub-volume area shown in red.

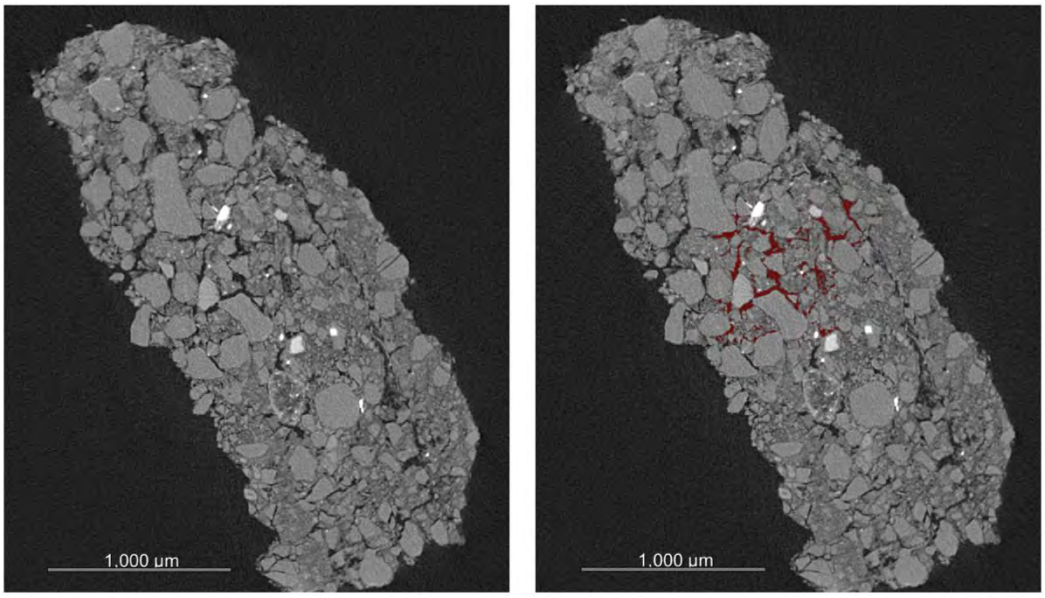

Figure A6: Left: XY view of VYD 984 sample in greyscale. Right: XY view of VYD 984 sample in greyscale with thresholding of pores in sub-volume area shown in red.

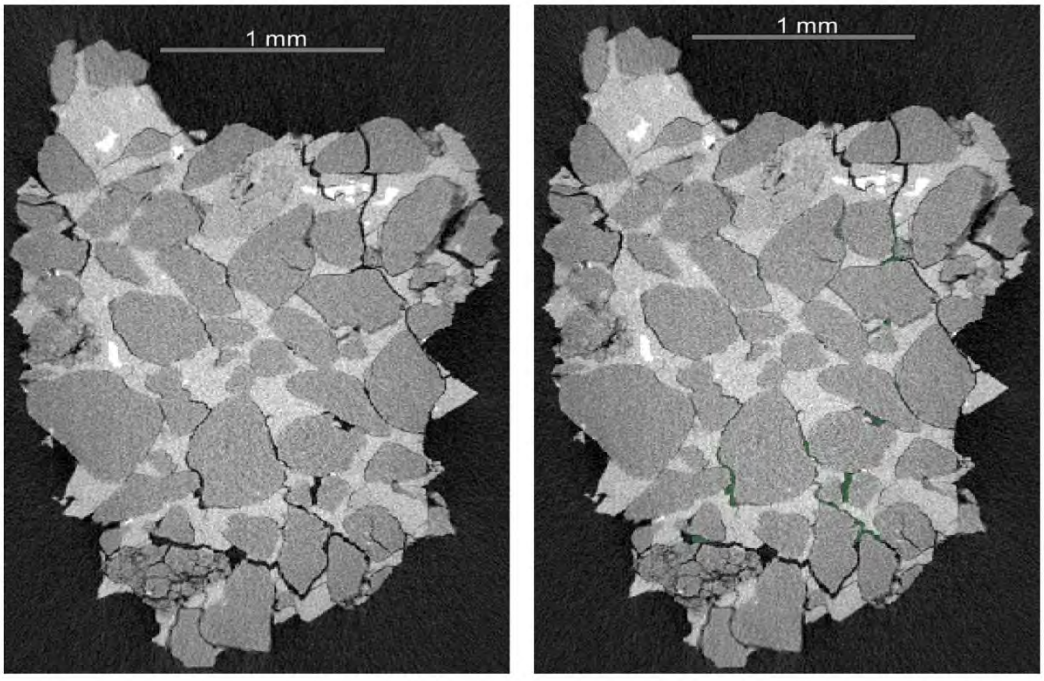

Figure A7: Left: XY view of VYD 987.6 sample in greyscale. Right: XY view of VYD 987.6 sample in greyscale with thresholding of pores in sub-volume area shown in green.

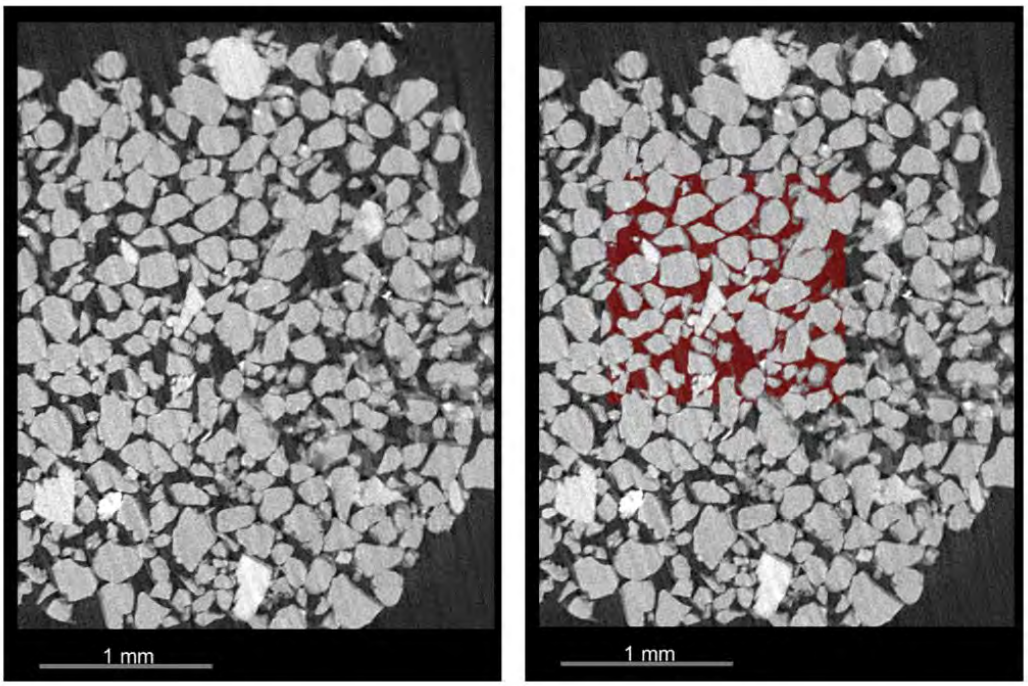

Figure A8: Left: XY view of A1 sub volume in greyscale. Right: XY view of A1 sub volume in greyscale with thresholding of pores in sub-volume area shown in red.

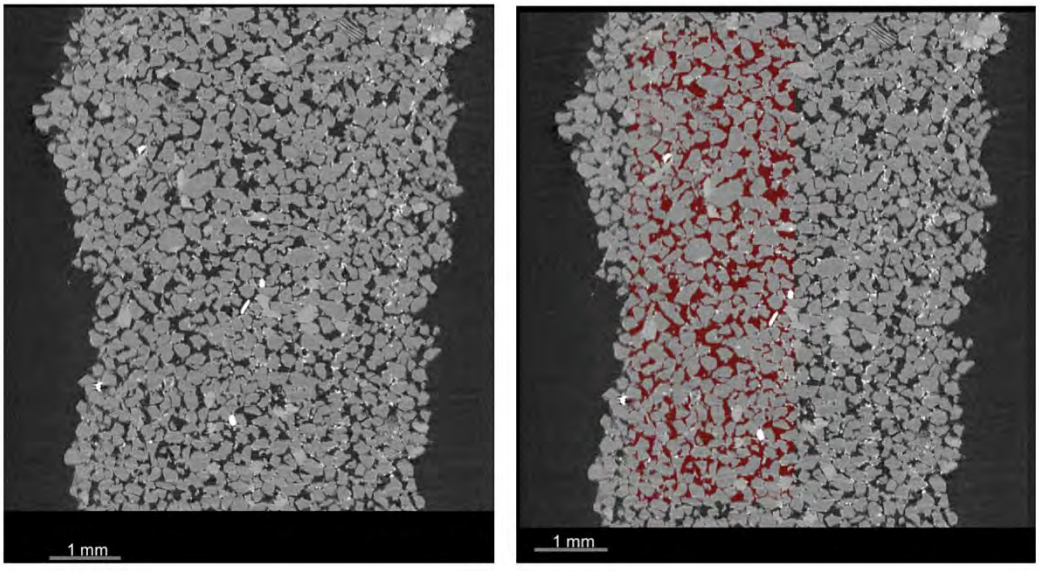

Figure A9: Left: XY view of E1 sub volume in greyscale. Right: XY view of E1 sub volume in greyscale with thresholding of pores in sub-volume area shown in red. Clay staining noted at outcrop. This is shown as the high density (white) minerals in the greyscale image.

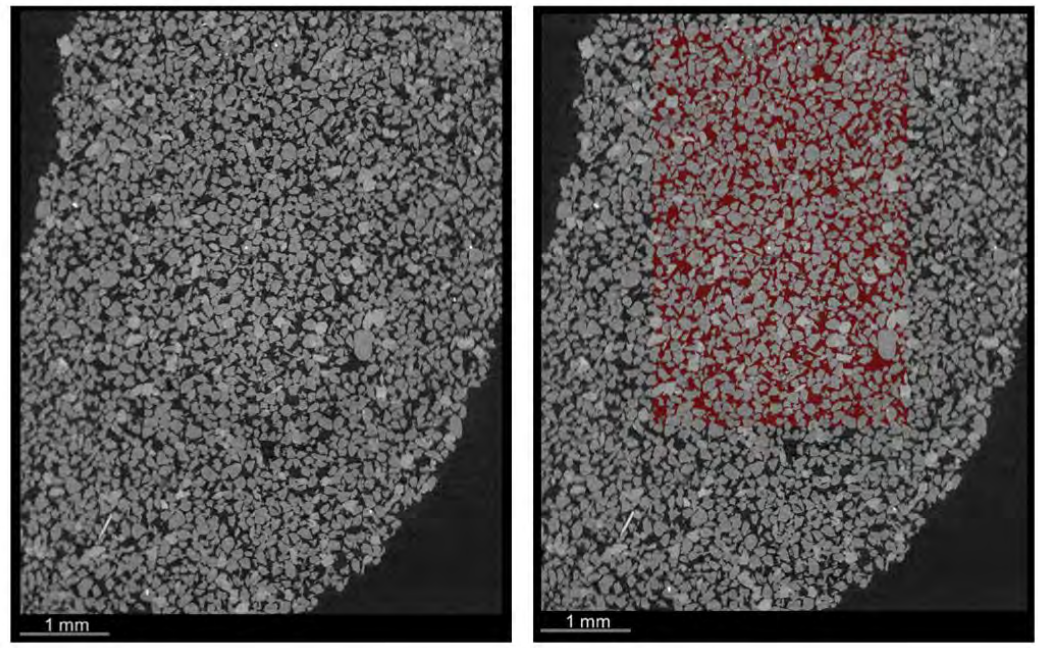

Figure A10: Left: XY view of V1 sub volume in greyscale. Right: XY view of V1 sub volume in greyscale with thresholding of pores in sub-volume area shown in red.

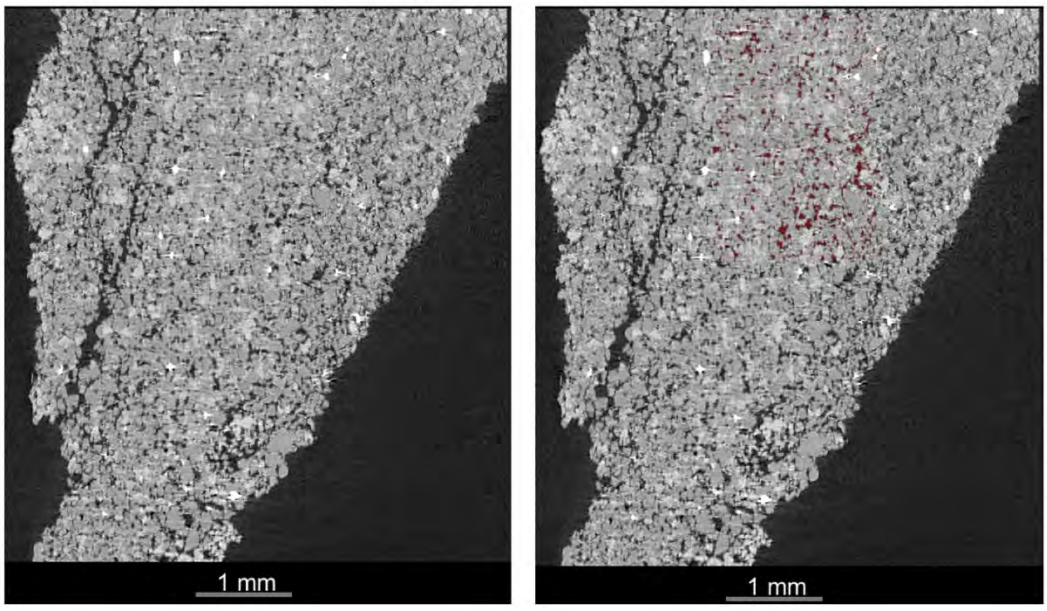

Figure A11: Left: YZ view of Z1 sample in greyscale. Right: XY view of Z1 sample in greyscale with thresholding of pores in sub-volume area shown in red. Fracture avoided from the analysis. Higher cementation observed.

5. Discussion and Conclusion

By using X-CT analysis, the aim of this work was to determine the porosity and provide an insight into the possible presence of pervasive clay minerals or carbonate cement blocking pore space within the sandstone samples. While the X-CT analysis can provide an indication of the porosity of each sample and show that there are different mineral phases contained in the sample, it must be paired with further petrophysical and mineralogical analysis to determine the mineral composition present in each sample. Nonetheless, this work provides an initial indication of the porosity and the mineralogical properties of the samples.

The conducted measurements show that the porosity within the Devonian sandstones in the Baltic region are higher at outcrop than they are at reservoir conditions in the Klaipeda-1I and Vydmantai-1 wells. However, the samples obtained from the Palanga-318 well show a greater similarity to those at outcrop and indicate less of an influence of cementation or clogging of pores with pervasive clay minerals. The X-CT scans show that the Klaipeda-1I well has a porosity of around 8.4%, with evidence of cementation and different mineral phases shown in the scan. This value of porosity is influenced by the scanning conditions and the size of the core sample and therefore should be considered as a conservative estimate of the porosity of this sample. The Vydmantai-1 samples are well cemented and initial estimates of porosity are of 3.11% and 9.60% respectively. X-CT scans of the Vydmantai-1 show evidence of abundant carbonate cement and that porosity is fracture dominated. The fractures are likely to be a result of sample preparation and are not representative of reservoir conditions, therefore we can expect these values of porosity to be optimistic. The Palanga-318 samples have an estimated porosity of 18% and 22% respectively, with less cementation and consolidation evident however some carbonate cement is observed.

Analysis of outcrop samples show that these samples are much less consolidated and have greater porosity than the borehole core samples, ranging from 23-28 % for the Amata and Burtneiki Formations (Samples, A1, E1, and V1). These samples are similar in porosity and mineralogical composition, indicated by similar mineral phases evident in the X-CT scans. Sample Z1, of the Amata Formation, has a reduced porosity of ~8% and higher cementation in comparison to the other outcrop samples. This sample was observed at outcrop as being fine grained sandstone diagenetically altered with greater carbonate cement content. There is a greater similarity between this sample reservoir conditions in the Viešvile Formation in the Klaipeda-1I and Vydmantai-1 wells.

This work indicates the importance of studying outcrop and core material from analogous Devonian sandstone formations to provide an insight to reservoir conditions at the Klaipeda geothermal site. It is recommended that the relationship between porosity and permeability and mineralogy should be assessed further by conducting experiments on the mineralogical composition of the samples.

REFERENCES

1. Brehme, M., Nowak, K., Banks, D., Petrauskas, S., Valickas, R., Bauer, K., Burnside, N., and Boyce, A. 2019. A Review of the Hydrochemistry of a Deep Sedimentary Aquifer and Its Consequences for Geothermal Operation: Klaipeda, Lithuania. Geofluids, 2019, pp. 20. https://doi.org/10.1155/2019/4363592

2. Brooks, R. A., and Di Chiro, G. 1976. Beam hardening in x-ray reconstructive tomography. Physics in Medicine & Biology, 21 (3), pp. 390-398.

3. Cnuddle, V., and Boone, M. N. 2013. High-resolution X-ray computed tomography in geosciences: a review of the current technology and applications. *Earth-Science Reviews*, 123, pp. 1-17. https://doi.org/10.1016/j.earscirev.2013.04.003

4. Ketcham, R. A., and Carlson, W. D. 2001. Acquisition, optimization and interpretation of X-ray computed tomographic imagery: applications to the geosciences. *Computers & Geosciences*, 27 (4), pp. 381-400. https://doi.org/10.1016/S0098-3004(00)00116-3

5. Kiipli, E., Kiipli, T., Kallaste, T., and Märss, T. 2016. Chemical weathering east and west of the emerging Caledonides in the Silurian – Early Devonian, with implications for climate. Canadian Journal of Earth Sciences, 53 (8), pp. 774-780. https://doi.org/10.1139/cjes-2015-0156

6. Noiriel, C. 2015. Resolving time-dependent evolution of pore-scale structure, permeability and reactivity using X-ray microtomography. Reviews in Mineralogy and Geochemistry, 80 (1), pp. 247-285. https://doi.org/10.2138/rmg.2015.80.08

7. Pipira, D., Kostjukovs, J., and Stinkulis, G. 2015. Mineral Composition and Morphology of Dolocretes of the Devonian Burtneiki and Amata Formations, Latvia. Material Science and Applied Chemistry, 2015/32, pp. 13-18. doi: 10.1515/msac-2015-0002

8. Zinevicius, F., Sliaupa, S., Mazintas, A., and Dagilis, V. 2015. Geothermal Energy Use in Lithuania. 2015. Proceedings of the World Geothermal Congress, Melbourne, Australia 19-25 April 2015. [Online]. Available at: https://pangea.stanford.edu/ERE/db/WGC/papers/WGC/2015/01054.pdf

9. Zinevicius, F., Sliaupa, S., Mazintas, A., and Nika, N. 2020. Geothermal Energy Country Update - Lithuania. Proceedings of the World Geothermal Congress, Reykjavik, Iceland April 26 – May 2, 2020. [Online]. Available at: https://pangea.stanford.edu/ERE/db/WGC/papers/WGC/2020/01069.pdf

Appendix B Experimental procedures for sample characterisation

Jin Ma, Xiang-Zhao Kong, Martin O. Saar

Geothermal Energy & Geofluids Group, Department of Earth Sciences, ETH-Zürich

The objective of this work is to provide input for geochemical numerical models, including sample chemical composition, mineral accessible surface area, sample porosity and permeability. Various laboratory measurements have been performed to characterize the pore space and mineral distribution of sandstone rock samples. Their mineral fractions and accessible surface areas were determined based on analyses of scanning electron microscope (SEM) images of sandstone thin sections. Their porosity and the pore size distribution were also measured to assist the SEM image analyses.

1. Rock samples

The sandstone rock samples were taken at a depth of 954.6 m in the geothermal well Vydmantai-1, at the southeast end of the Baltic Sea of Lithuania. Transmitted light microscopy observations show that these sandstone samples consist of well-rounded, fine to very fine grains (sizes of 65μm - 250μm), composed of quartz, feldspar, mica, and a carbonate mineral (Figure B1).

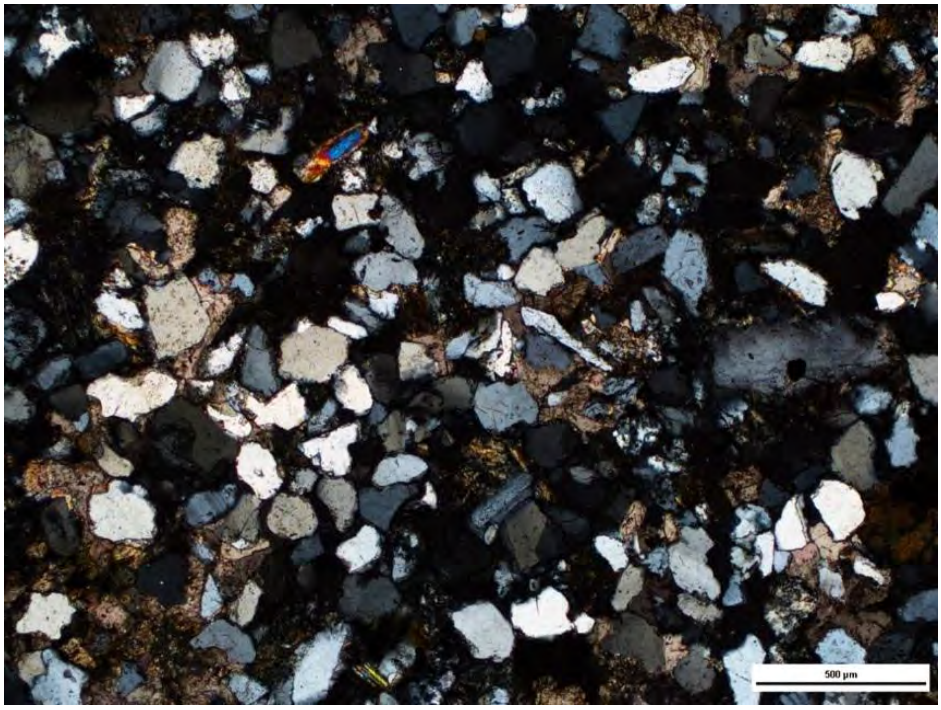

Figure B1: Transmitted light microscopy of a sandstone thin section.

Sandstone specimens of various types, such as cylinder, thin section and chip, were prepared for various laboratory analyses. For example, a cylindrical rock specimen with a diameter of 25.4 mm and a length of 39.0 mm was cut for 3D micro-CT imaging, porosity measurements, and reactive flow-through experiments (Ma et al., 2019a). A 35 μm-thick thin section with a size of 11.37 mm x 8.34 mm was sliced for microscopy measurements, such as SEM-BSE imaging and SEM-EDS element mapping. Here BSE refers to the backscattered electron, and EDS refers to the energy dispersive X-ray spectroscopy.

2. Porosity, pore size distribution (PSD) and permeability

The pore volume of the cylindrical specimen was measured using the Micromeritics AccuPyc II 1340 Pycnometer in the Rock Deformation Laboratory at ETH Zurich. The solid volume of a cylindrical sandstone specimen was determined to be 15.441 ±0.004 ml after 16 purges of Helium at a temperature of 25.14 °C. The total specimen volume was calculated to be 19.7 ±0.1 ml, given its diameter of 25.4 ±0.1 mm and length of 39.0±0.1 mm. Then the specimen porosity of 21.9 ±0.4 % was calculated as one minus the solid fraction (i.e., the ratio between the measured solid volume and the total specimen volume).

Pore (or throat) size distribution (PSD) was obtained by Mercury intrusion porosimetry. The PSD measurement was carried out at a temperature of 22.6 °C and a maximum pressure of 400 MPa using the Porotec Pascal 140 and 440 (with a detectable size range of 2 nm-100 μm in diameter) in the IGT Claylab at ETH Zurich. Independent analysis of porosity and PSD of the 35 μm-thick thin section was also performed using various image-processing techniques. The thin section was continuously scanned in 10 x 10 windows using a Jeol JSM-6390 LA SEM together with a BSE detector in the Electron Microscopy Lab at ETH Zurich. The scanning was performed at an electron accelerating voltage of 15 keV at a working distance of 10 mm to obtain a 1.2 μm-resolution. These 10 x 10 grayscale SEM-BSE coherent images were then stitched using ImageJ to generate a full image of 9474 x 6947 pixels, as shown in Figure B2(a). Figure B2(b) shows the corresponding binary image (pores in black and solid in white) using a threshold of 70 on a grayscale of 0 to 255 (black to white, see the inset with a grayscale histogram at the top right). This binary image was then used for porosity, PSD, and mineral specific surface area (SSA) analyses. According to the principle of stereology (Weibel, 1969), the 2D area density mm^2/mm^2 is equivalent to the 3D volume density mm^3/mm^3. After segmentation of pore space from the binary image, we calculate the sample porosity as the 2D areal density mm^2/mm^2 of pores with respect to the total image size (area). PSD of the segmented pores was also determined using the Xlib plugin of ImageJ with a continuous PSD calculation. Micro-computed tomography (CT) was employed to obtain a 3D geometric representation of the sandstone sample at Scanco Medical AG, Brüttisellen, Switzerland. Cross-section images with 9.5 μm-resolution were acquired using an energy of 130 kV and a current of 61 μA. The number of projections was 2000 and the integration time was 3.74 s. Collected projections were reconstructed to produce 3D CT data and PSD of the 3D reconstructed pore space was analysed using Scanco Medical's Proprietary software (Hilderbrand et al, 1997).

Figure B3 shows the PSDs from mercury intrusion measurements (blue solid line), calculations using the SEM image (red solid line) and the 3D CT data (black dashed line). The mercury porosimetry PSD shows a detectable range of 0.01 – 100 μm with a peak at a pore (throat) size of 15 μm. The SEM image PSD shows a detectable range of 1.2 – 80 μm with a peak at a pore size of 30 μm. In addition to image resolution issues, the discrepancies between the curves is very likely introduced by the difference in measuring principles employed by these two methods, i.e., the mercury porosimetry method better reflects the pore throat size, while the image analysis method is more sensitive to the total pore area. The above PSD results are also partially confirmed by the PSD from the 3D micro CT analysis. Due to the limitation of current computational resources, the resolution of the 3D CT image was first up-scaled to 19.5 μm before the PSD was determined. For this up-scaled resolution, most small pores have been filtered-out so that only 16% (relatively large) pores remain, leaving only the pores bigger than 39 μm. Nonetheless, the PSD from the analysis of 3D CT data matches well with PSD from the analysis of 2D SEM data. This confirmation strongly suggests that the stereological method, used in this study, is valid. However, further analysis of smaller pore sizes in the 3D CT data is recommended.

The sandstone bulk permeability was measured with brine (1 mol/L) using flow-through experiments on a core with a diameter of 25.4mm and a length of 39 mm. The test flow rates range from 0.5 to 8 ml/min, yielding a bulk permeability of 356 mD using Darcy's law.

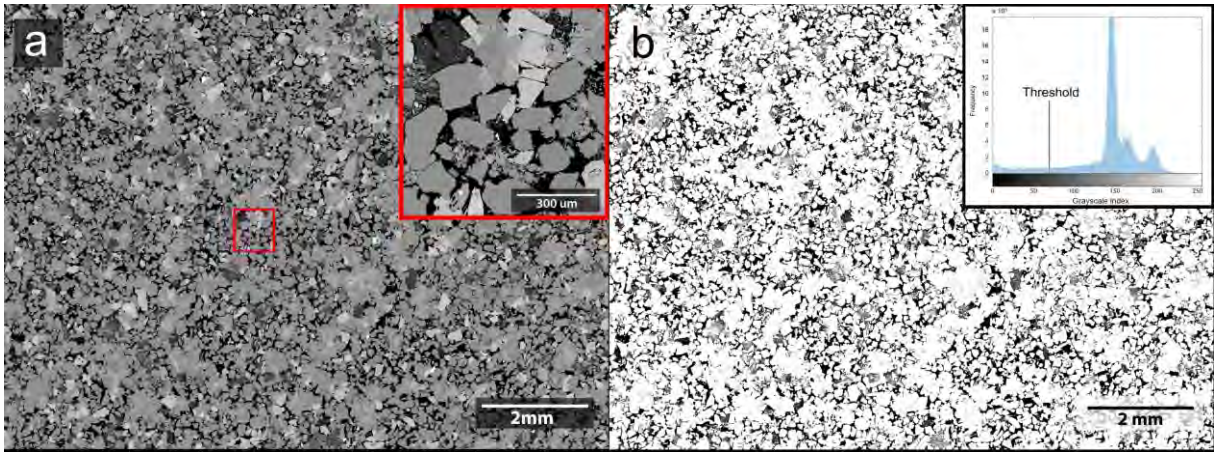

Figure B2: Analysis of the SEM-BSE image: (a) the grayscale SEM-BSE image with a resolution of 1.2 μm, enlarged by a factor of 5 (inset in the right-upper corner) of the red square; (b) the corresponding binary image (black represents pores and white represents solid) with the inset showing a gray-value histogram and the applied threshold.

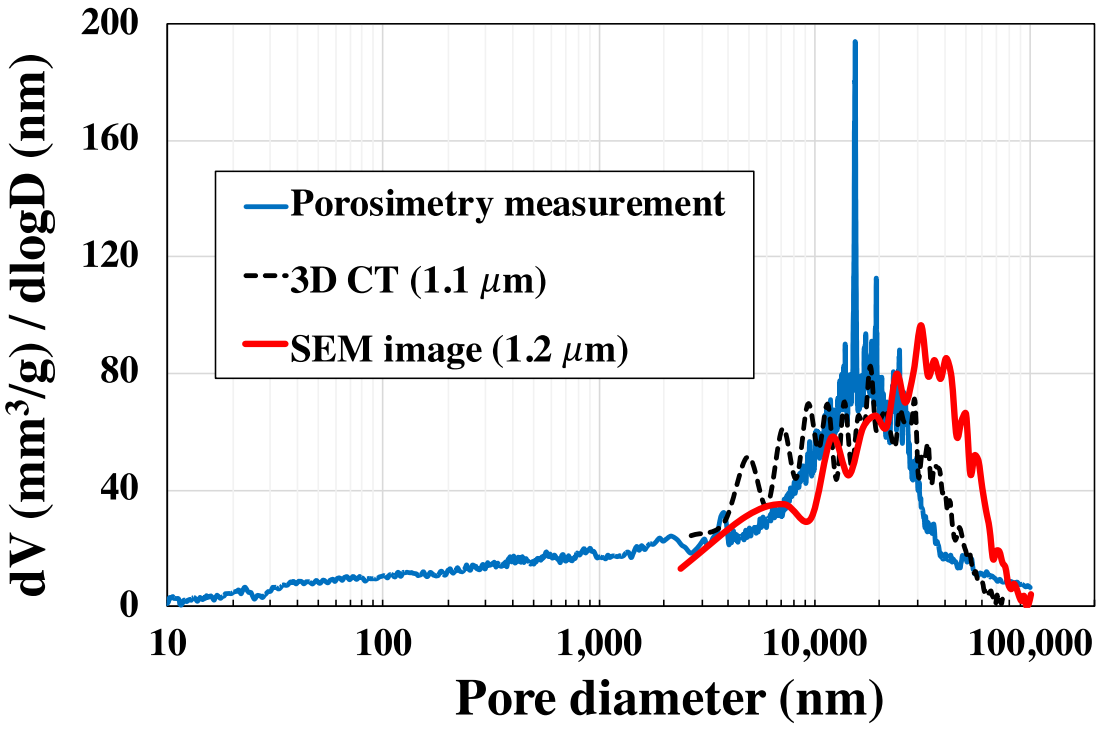

Figure B3: Pore size distribution (PSD) calculated from mercury intrusion porosimetry, SEM image, and 3D CT data.

3. Mineralogy analysis

Sandstone compositions were determined using a combination of different techniques, including X-ray fluorescence (XRF), X-ray diffraction (XRD), SEM element mapping, and SEM quantitative chemical analysis. To ensure representative measurements on compositions, 24.4 g of the sandstone sample was crushed into fine powder for both XRF and XRD analyses.

The XRF analysis was performed using an XRF spectrometer (WD-XRF, PANalytical AXIOS) in the high-pressure Lab at ETH Zurich. During the XRF measurement, 1.5 g of the crushed powder was mixed with 7.5 g of Lithium-Tetraborate (at a mass ratio of 1:5) using a Claisse M4® fluxer. The mixture was processed with a procedure of Loss on Ignition (LOI) at 1050°C for 2 hours and then melted at 1080°C using the PANalytical Eagon 2 fusion instrument. Weight percentages of 10 major oxides (SiO_2, TiO_2, Al_2O_3, Fe_2O_3, MnO, MgO, CaO, Na_2O, K_2O, P_2O_5) and of 21 trace elements (S, Sc, V, Cr, Co, Ni, Cu, Zn, Ga, Rb, Sr, Y, Zr, Nb, Ba, La, Ce, Nd, Pb, Th, U) were measured during the XRF test. These weight percentages were calibrated with ca. 30 certified international standards with emphasis on igneous and metamorphic rock compositions.

The XRD analysis was performed with a Powder X-ray Diffractometer (Bruker AXS D8 Advance) and a Lynxeye superspeed detector in the high-pressure lab at ETH Zurich. The detected spectrum was analysed using ICDD PDF-2 (Version 4.15.3.4) with the Database Version 2.1502. The XRD analysis indicates that crystalline mineral phases of the sandstone were identified as quartz, dolomite, K-feldspar (orthoclase), muscovite, kaolinite and ilmenite. However, this XRD analysis is a semi-quantitative measurement. To obtain quantitative mineral composition in weight percentage, we need to combine the XRD and the XRF results. Taking typical densities of identified minerals (The engineering toolbox: http://www.engineeringtoolbox.com/mineral-density-d_1555.html), we summarize mineral volume fractions of the sandstone in Table B1. Here mineral chemical formulas were confirmed with both XRD and quantitative SEM analysis.

The quantitative SEM analysis was carried out with the Jeol JSM-6390 LA SEM and an EDS system, Thermo Fisher NORAN NSS7, in the high-pressure lab at ETH Zurich. Elements were mapped on the SEM image with a pixel resolution of 2.4 μm using a 30 mm^2 Silicon-drift detector (SDD). The element-wise pixels were registered according to elemental X-ray spectra at 20 sec x 50 frames (1000 counts). Similar to the SEM-BSE analysis, the same area of the sandstone thin section (11.37mm x 8.34 mm) was continuously imaged with 5 x 5 windows during the EDS scanning. The resultant 25 coherent images were stitched using ImageJ to produce a full image of 4737 x 3474 pixels. This EDS image was then overlaid on the SEM image to produce a combined SEM-EDS image of mineral distribution (Figure B4). To estimate the average chemical formula of individual minerals as summarized in Table B1, we calibrated the X-ray beam current using a Farady-cup, determined element ratios on several selected spots on the image, and integrated the previous XRD results.

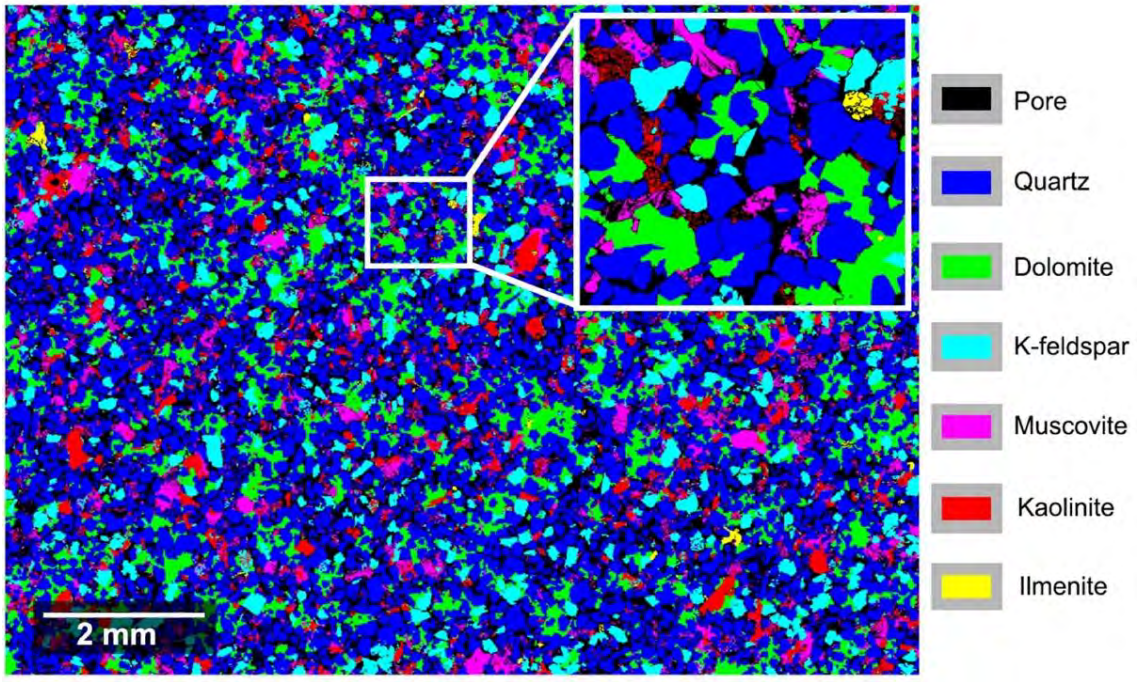

Figure B4: Mineral distribution of the sandstone.

Table B2: Minerals and their chemical formula, identified using a combined XRF-XRD method and SEM image processing. The mineral densities are from the engineering toolbox: http://www.engineeringtoolbox.com/mineral-density-d_1555.html

Mineral	**Average chemical formula**	**Density** g/cm^3	**XRF+XRD** vol.%	**SEM** vol. %
Quartz (Qtz)	SiO_2	2.62	47.65	45.53
Dolomite (Dol)	$CaMg_{0.77}Fe_{0.23}(CO3)_2$	2.84	12.36	12.22
K-feldspar (Ksp)	$KAlSiO_3$	2.56	11.82	9.93
Muscovite (Mu)	$K_{0.85}Na_{0.15}Al_2(AlSi_3O_{10})(OH)_2$	2.82	5.38	4.76
Kaolinite (Kln)	$Al_{1.9}Si_{2.1}O_5(OH)_4$	2.60	0.91	5.64
Ilmenite (Ilm)	$Fe_2Ti_5O_{12}$	4.72	0.23	0.27

4. Surface area analysis

Mass-specific surface areas (SSA) of rock samples were measured using a gas adsorption method based on the Brunauer–Emmett–Teller (BET) theory. The measurements were conducted using a surface area analyser, Quantachrome Autosorb 1MP, in the Claylab at ETH Zurich. Before BET measurements, small pieces of sandstone samples (in total 3.6 g) were vacuumed at 150°C for about 15 hours. During the BET measurements, we employed nitrogen as the adsorption gas at a temperature of 77.3 K, and a 5-point method which yielded a bulk specific surface area (SSA) of 1.447 m^2/g with a correlation coefficient of 0.99995.

Using the 2D binary SEM-BSE image (at a resolution of 1.2 μm) shown in Figure B1(b), one can independently calculate the digital perimeter density (μm/μm^2), i.e., the ratio between the 2D solid (i.e. minerals) perimeter and the 2D solid area. Based on the principle of stereology (Weibel, 1969), SSA (m^2/g) at a resolution of 1.2 μm was then the product of a bias correction factor of $4/\pi$, the bulk rock density (measured as 2.11 g/cm^3), and the digital perimeter density.

The overlaid mineral distribution (Figure B4) obviously allows the determination of the SSA of individual minerals, in particular the SSA of individual minerals exposed to pore space, i.e., the accessible specific surface area (SSA) of each mineral. However, there is a resolution difference between the BET measurement (at atomic scale) and the SEM-EDS image (a resolution of 2.4 μm). In order to bridge the resolution gap, we developed a novel joint method that appropriately down-scales individual image-based accessible surface areas (ASA) with the support of Brunauer-Emmett-Teller (BET) measurements and a Monte-Carlo algorithm (Ma et al., 2019b). First, we segment pore space and mineral phases in the Scanning Electron Microscopy (SEM) image and compute the image-based surface areas for individual minerals. During this step, two types of image-based SSA are defined: the accessible surface area (ASA) and the grain surface area (GSA). The ASA is defined as the surface area exposed to the pore space. The sum of the ASA should equal the SSA from the BET measurements. The GSA is the total surface area of all segmented grains of individual minerals in the SEM image, which should fall in the range of BET-measured SSAs of the crushed grains of individual minerals. The image-based ASA of each mineral is calculated as the ratio of the interface pixels between the mineral and the pore space to the total image pixels. The image-based GSA of each mineral is calculated as the ratio of the total contour pixels of all segmented grains of this mineral to the total number of pixels occupied by this mineral. Then, to account for the sub-pixel scales in these image-based ASAs, a set of mineral-specific scaling factors (SFs) are determined, using a Monte-Carlo algorithm, where: (1) the sum of the individual products of the image-based ASAs and SF is benchmarked against the BET measurements that determine the total ASA of the sandstone specimen: $\mathrm{SSA}_{tot} = \sum_{i=1}^{i=N} \mathrm{SF}_i \times \mathrm{ASA}_i$ and $\mathrm{BET}_{tot,min} \leq \mathrm{SSA}_{tot} \leq \mathrm{BET}_{tot,max}$, (2) the GSA of each mineral is constrained by the SSA of crushed grains of this mineral, measured using the BET method and reported in the literature: $\mathrm{BET}_{i,min} \leq \mathrm{SF}_i \times \mathrm{GSA}_i \leq \mathrm{BET}_{i,max}$; and (3) a most probable SF for each mineral is determined, using the Monte-Carlo algorithm, based on the probability map of the SF. Here *i* indicates the *i*-th mineral among the total number of minerals, *N*, in this sandstone. This Monte-Carlo approach yields individual scaling factors for each mineral, such that the accessible SSA of each individual mineral is calculated as the product of its scaling factor and its exposed surface area, acquired from the SEM-EDS image (Table B2).

The stereological analysis of the SEM images yields an image-based SSA of 0.042 m^2/g, while the BET-measured SSA is 1.6700$\pm$0.0019 m^2/g. After the segmentation of mineral phases, the image-based ASAs and GSAs for each mineral are calculated and listed in Table B2. By multiplying the most probable SF, obtained from the Monte-Carlo analysis, both the image-based ASA and the GSA can be downscaled to the same resolution as that of the BET measurements. As expected, the corrected GSA falls into the range of SSAs for a single mineral, reported by previous studies, using BET measurements on crushed grains. As shown in Table B2, the surface roughness correction significantly increases the surface area fractions of the clay minerals, such as kaolinite. For a mass fraction of 7.9 % of kaolinite, it provides 81.2 % of the total SSA of the sandstone specimen. This result is rational, as clay minerals usually accommodate large amounts of micro-features, much smaller than the SEM image pixel size (1.2 μm). In contrast, quartz only provides 7.3 % of the total SSA, while it comprises 58.4 wt. % of the specimen. After the correction of surface roughness, the ASAs of muscovite and dolomite are also considerably elevated, compared to their image-based values, due to their flaky and porous features.

Table B3: Surface roughness correction for the GSA and ASA

	Qtz	Dol	Ksp	Mu	Kln	Ilm	Total
GSA from image m^2/g	0.041	0.047	0.053	0.100	0.232	0.078	
ASA from image m^2/g	0.0173	0.0030	0.0034	0.0038	0.0149	0.0004	0.042
GSA from BET Lit. m^2/g	0.02-0.55	0.07-1.96	0.08-0.25	0.66-5.53	13.2-78.0		
SF applied to SSA	7.00	21.79	3.09	30.90	91.00	3.69	
Corrected GSA m^2/g	0.287	1.024	0.164	3.090	21.112	0.288	
Corrected ASA m^2/g	0.121	0.065	0.011	0.117	1.356	0.001	1.670

5. Discussion and conclusions

The conducted measurements successfully characterize the hydraulic and chemical properties of the sandstone sample from borehole Vydmantai-1. The sandstone has a high bulk porosity of 21.9% and a relatively high permeability of 356 mD. The sandstone contains about 12 vol.% dolomite cement, which is recognized as the most reactive phase in this sandstone. About 40% of the dolomite surface area, i.e., ~0.065 m^2 per gram of sandstone, are exposed to pore space, indicating a high potential of dissolution during acid stimulation. The determined parameters provide critical inputs for geochemical models of Klaipeda area, but the relationship between mineral dissolution and permeability evolution needs to be further studied.

REFERENCES

1. Hildebrand, T., Ruegsegger, P., 1997, A new method for the model-independent assessment of thickness in three-dimensional images. Journal of Microscopy: 185, 67–75.
2. Ma, J., Querci, L., Hattendorf, B., Saar, M. O., & Kong, X. Z., 2019a, Toward a spatiotemporal understanding of dolomite dissolution in sandstone by CO_2-enriched brine circulation. Environmental Science & Technology. DOI: 10.1021/acs.est.9b04441.
3. Ma, J., Saar, M. O., & Kong, X. Z., 2019b, An image-and BET-based Monte-Carlo approach to determine mineral accessible surface areas in sandstones. DOI: 10.31223/osf.io/dhygb.
4. Weibel, E.R., 1969, Stereological Principles for Morphometry in Electron Microscopic Cytology. International Review of Cytology: 26, 235-302.

Appendix C Numerical predictions of chemical treatment performance in geothermal reservoirs

Laura J. Wasch and Brecht Wassing

Applied Geosciences Department, TNO

1 Introduction

Both acid injection and soft-stimulation by CO_2 co-injection were studied by means of numerical modelling using reactive transport models (RTM) and thermo-hydraulic-mechanical-chemical (THMC) coupled models. Acid injection can be applied to clean up the near-well reservoir after drilling or to improve the initial flow properties (Ali et al., 2016, Portier et al., 2007, Rea and Di Lullo, 2003). Different materials could be responsible for clogging the pores, including reservoir fines, corrosion products, scale particles or in situ precipitated minerals induced by chemical interaction between the injected brine and reservoir (Ungemach, 2003, Boch et al, 2017). Reservoirs can also be initially clogged with cementing minerals such as carbonates. The current study is focussed on the latter case and aims at improvement of the initial permeability of a geothermal reservoir. Furthermore, the chemical interaction of the injected fluid and host rock and formation water are taken into account, possibly forming precipitates in the pore space.

The simulations of acid stimulation are focussed on the impact of HCl injection. Although sandstones are commonly stimulated with mud acid (HF and HCl), our focus on dissolving only the carbonate cements in the sandstones would not require HF. By using only HCl, complex interaction between HF and the host rock and formation brine is prevented. This also simplifies the modelling since a pre-flush (fluid stage pumped ahead of the main treating fluid) to displace the formation brine containing dissolved Na^+, Ca^{2+} or K^+ and prevent the formation of alkali-fluosilicates (Portier et al., 2007) is not required. This leaves only the main acid flush for the modelling, since an over flush (which is usually done to displace the non-reacted acid and reaction products into the formation after the main flush) is then also not required.

Besides acid stimulation, soft-chemical treatment could be accomplished by continuously injecting CO_2 acidized water (Wasch et al., 2020). The impact of CO_2 co-injection with the cold geothermal water is compared to the impact of acid stimulation by HCl. Geothermal reservoirs containing dissolved CO_2, often in addition to dissolved hydrocarbons, can experience CO_2 outgassing during geothermal water production due to pressure decrease. CO_2 outgassing disturbs the chemical equilibrium of the water, increases the water pH and frequently causes carbonate scale precipitation in surface installations (Wasch, 2014, Alt Epping). Alternatively, similar alterations of the water chemistry, increasing the acidity, could stimulate mineral dissolution and enhance the reservoir flow properties. Dissolving the captured CO_2 in the cold return water prior to injection could stimulate dissolution and enhance the injectivity of formations, while contribute to reducing CO_2 emissions at the same time. Stimulation of the reservoir by increasing the CO_2 content has been shown by experiments with CO_2-saturated brine on Rotliegendes sandstone. A permeability increase by a factor of two was found due to the dissolution of anhydrite and calcite (Huq et al., 2015). A numerical study showed that soft stimulation of the reservoir by enhanced calcite (and siderite) dissolution could yield a large porosity increase from 18 to 29 % and a considerable permeability improvement from 750 mD to 3.75 D around the injection well (Wasch et al., 2020). These studies show that there is a considerable potential for increasing reservoir permeability by injecting a CO_2 enriched fluid.

2 Numerical methods

2.1 RTM and THMC simulators

A reactive transport model (RTM) was developed using TOUGHREACT software Version 3 (Xu et al., 2006; Xu et al., 2014). The simulator introduces reactive chemistry into the TOUGH2 simulator on multiphase and multicomponent fluid flow in porous and fractured media (Pruess et al., 1999). We used the ECO2N fluid property module which includes the thermodynamic and thermophysical properties of H_2O - NaCl - CO_2 mixtures (Pruess, 2005). The ECO2N equation of state covers fluid properties for conditions of 10 °C < T < 300 °C, P < 600 bar, and salinity up to halite saturation. Geochemical simulations require a thermodynamic database containing parameters for mineral solubility and equilibrium constants. Several databases are available for TOUGHREACT and can be user selected. We used the geochemical database Thermoddem (V1.10_06Jun2017) developed by the BRGM (Blanc et al., 2012; http://thermoddem.brgm.fr/). The reaction of minerals is kinetically controlled using a rate expression of Lasaga et al. (1994) which is programmed into TOUGHREACT. Mineral kinetics are included using the reaction rates of Palandri and Kharaka (2004), which have to be provided as input for TOUGHREACT.

The coupled thermo-hydraulic-mechanical-chemical (THMC) model uses the software TOUGHREACT-Flac3d. The coupling between the TOUGHREACT V3 and FLAC3D is an iterative coupling: TOUGHREACT V3 is used to compute the evolution of flow, temperature and chemistry during injection into the reservoir. Pressure and temperature are then passed to FLAC3D. The mechanical response of the rocks, due to changes in pore pressure and temperature is computed in FLAC3D (https://www.itascacg.com). Mechanical stress changes and deformation (both volumetric and shear) are then used to compute changes in porosity and/or permeability changes (e.g. due to the tensile or shear-dilatant opening of fractures), which are passed back to TOUGHREACT, which solves the next reactive flow step. The software can handle both porous and fractured media. We extended the original code by Taron et al. (2010) to include the ECO2N equation of state of TOUGHREACT V3. The model has been extended such that it can include the coupling between flow and mechanics during acid injection and the resulting mineral (e.g. carbonate/anhydrite) dissolution and changes to the pore space. The model can be used to assess the coupled effects of the pressure and temperature development, mineral dissolution and mechanics on porosity and permeability evolution, the potential mechanical degradation of strength and associated compaction and the potential of thermal fracturing near the injection well. Section 2.2 shortly describes the setup of the model. At this stage, the software has been used for a number of trial runs only. Future experimental studies should provide insight and data on the relation between the dissolution of cement, porosity changes and the mechanical strength of rock samples, which can then serve as input to the coupled THCM models.

2.2 RTM Field-scale geothermal reservoir model

The software Petrasim was used for TOUGHREACT Pre- and post-processing. A polygonal mesh was created of 1.5 by 3 km (Figure C1). For the maximum cell size, an area 1250.0 m² was chosen and for the maximum cell area near well a value of 0.01 m^2 was selected. The default value of 30° was used for the minimum refinement angle. With these input values, a mesh of 38196 cells was created. This mesh has finer cells near-well of roughly 15 cm in diameter. Two vertical wells are defined with Well 1 (x 750 m, y 750 m) and Well 2 (x 2250 m, y 750 m) 1.5 km apart at reservoir level. The boundary conditions are assumed to be closed. Several layers were defined, but this work focusses on six reservoir layers with a top at 2300 m and a base at 2700 m.

We used the reservoir conditions as reported in Wasch et al. (2020). The initial reservoir pressure is 255 bar with a temperature of 88 °C. The model is initialized for 100 years to equilibrate the pressure and temperature over the reservoir depth. With the reservoir pressure of 255 bar, the pressure at the top of the model becomes 280 bar and the bottom pressure 246 bar (Figure C).

The layers have various rock properties but are initially homogeneous within one layer. The reservoir has a porosity of 18% and a permeability of 7.5E-13 m² (750 mD). Although this reservoir is of good quality, it is used as an example to study chemical treatment. Mineral reactions can have an effect on the volume of minerals and hence change the porosity. Porosity changes are calculated using mineral the specific molar volumes included in the thermodynamic database. The porosity , the permeability is altered. We used the porosity-permeability relationship of Verma and Pruess (1988). With a critical porosity of 85% of the initial porosity and a power law component of 4 (formula C1). These values are average values used for porous media (Hommel et al., 2018).

$$\frac{k}{ki_i} = \left(\frac{\phi - \phi_c}{\phi_i - \phi_c}\right)^n \qquad \text{(C1)}$$

Where *k* is the permeability, *ki* the initial permeability, *φ* the porosity, *φi* the initial porosity, *φc* the critical porosity below which the permeability goes to zero, and *n* is a power law exponent.

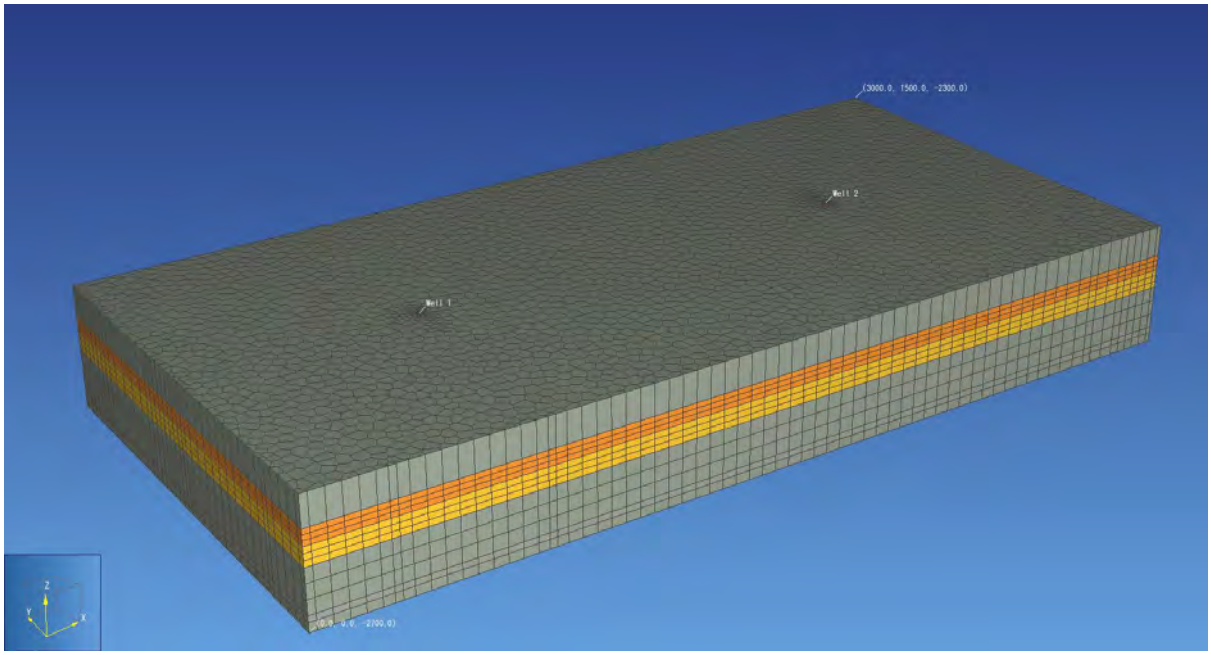

Figure C1. The polygonal 1.5 by 3 km mesh with smaller cell sizes around the two wells.

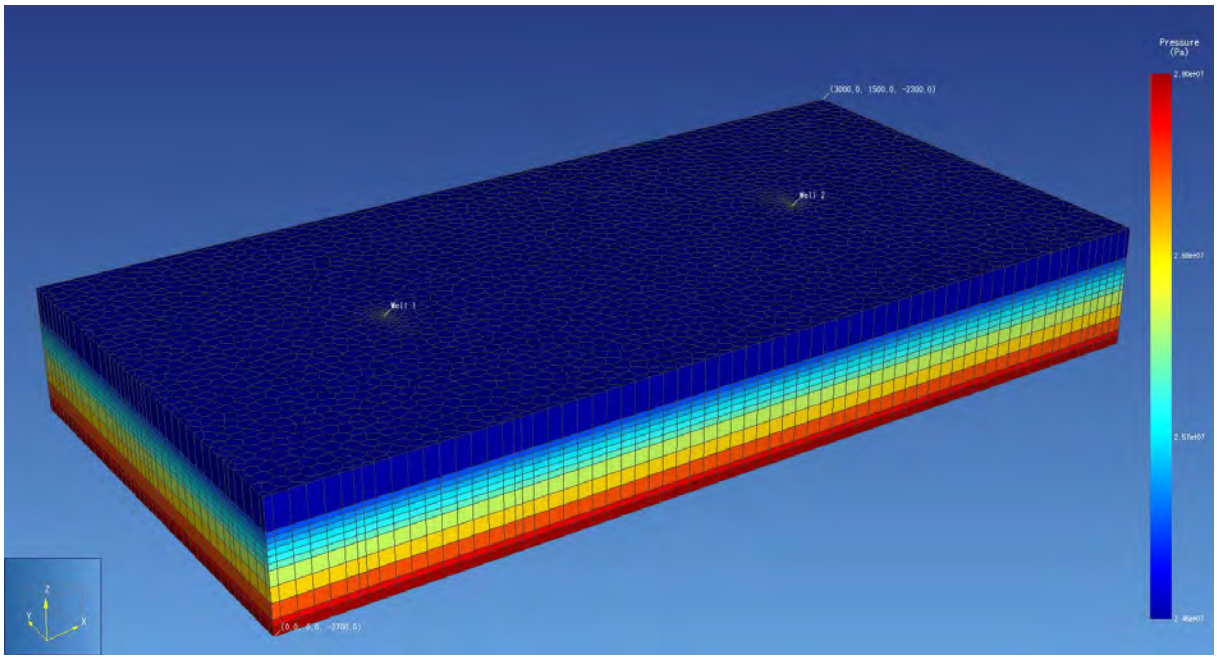

Figure C2. Pressure distribution in the geothermal reservoir model after 100 years of initialization

The base case injection temperature is 30 °C. Many Dutch doublets co-produce CH_4 and CO_2 with the water, which are dissolved in the water at reservoir conditions but degas upon ascend. The pressure in the surface installation (gas separator tank) can be kept under pressure to outgas and utilize most of the methane but keep a fraction of CO_2 in solution. Keeping an amount of CO_2 in solution is required to limit the pH increase and prevent calcite scaling (Alt-Epping et al., 2012, Wasch, 2014). As reported in Wasch et al. (2020), the calculated initial amount of CO_2 in the reservoir is 2.29E-02 mol/l, which is the measured dissolved CO_2 (1.43E-02 mol/l) plus the total separated CO_2 at standard conditions (8.61E-03 mol/l). This yields a dissolved mass fraction of CO_2 of 9.05E-04 (=n MCO_2/(1000 + m MNaCl + n MCO_2)) as used in TOUGHREACT. For re-injection, a CO_2 concentration value of 1.938E-02 mol/l was used, which is the CO_2 concentration in the reservoir (2.29E-02 mol/l) minus the separated CO_2 (3.57E-03 mol/l). We used a salinity in TOUGHREACT with an Xs value of 0.1 (Xs=m*MNaCl/(1000+m*MNaCl)), based on a measurement of 38800 mg/L Na^+ and 75710 mg/L Cl^-. With a simplified constant well flow of 150 m^3/h water, the injected masses were calculated (table C1). Injection is defined for each component of the fluid separately while production is defined by a mass equal to the sum of the injected components. For acid stimulation we assume a concentration of 15 wt% HCl (4.4 mol/l).

The mineralogy as used in TOUGHREACT is listed in table C2. The measured water composition from geothermal water is initialized in TOUGHREACT with the measured exsolved CO_2 at reservoir conditions. The water composition obtained after equilibration with the reservoir minerals is listed in table C3.

Table C1: Injection and production data.

	Component	Rate (kg/s)	Enthalpy (J/kg)
Injection	Water	41.67	148800
	Salt	4.771	-
	CO_2	0.036	252100
Production	Mass	-46.477	-

Table C2: Reservoir mineralogy.

Mineral	quartz	calcite	siderite	pyrite	kaolinite	smectite(MX80)
Formula	SiO_2	$CaCO_3$	$FeCO_3$	FeS_2	$Al_2Si_2O_5(OH)_4$	$Na_{0.409}K_{0.024}Ca_{0.009}(Si_{3.738}Al_{0.262})(Al_{1.598}Mg_{0.214}Fe_{0.208})O_{10}(OH)_2$
Volume Fraction	0.616	0.101	2.54E-03	4.0E-04	1.85E-02	1.22E-02

Table C3: Equilibrated water composition.

Element	H^+	Ca^{+2}	Mg^{+2}	Na^+	K^+	H_4SiO_4	HCO_3^-	SO_4^{-2}	Al^{+3}	Cl^-	Ba^{+2}	Fe^{+2}
Concentration (mol/l)	1.19E-02	0.175	4.61E-02	1.92	1.94E-02	7.41E-04	1.86E-02	7.06E-03	2.34E-08	2.37	2.11E-05	1.47E-03

2.3 THMC Radial geothermal reservoir model

Figure C3 shows the basic geometry of the coupled THCM model for simulation of acid injection. The model comprises a quarter symmetry of an injection well, surrounded by a porous sandstone reservoir. Vertical boundaries are fixed, which means plane strain conditions are modelled, vertical boundaries are modelled as no flow boundaries. The model is one element thick, simulating radial flow from an injection well over the entire height of a sandstone reservoir. Boundary conditions for the injection well can be chosen such that either an open hole section (with no displacement constraints), or a cased borehole can be modelled in FLAC3D (in which case displacement constraints are imposed inside the well). In case of modelling an open hole section, a bottom hole pressure is imposed inside the injection well, which is at all times equal to the pore pressures that builds up in the elements bounding the injection well. Fluid is injected into the elements bounding the injection well, at varying rates and temperatures. During acid injection, the evolution of pressures, temperatures, porosity, permeability, stress and elastic and plastic (inrecoverable) strain can be monitored.

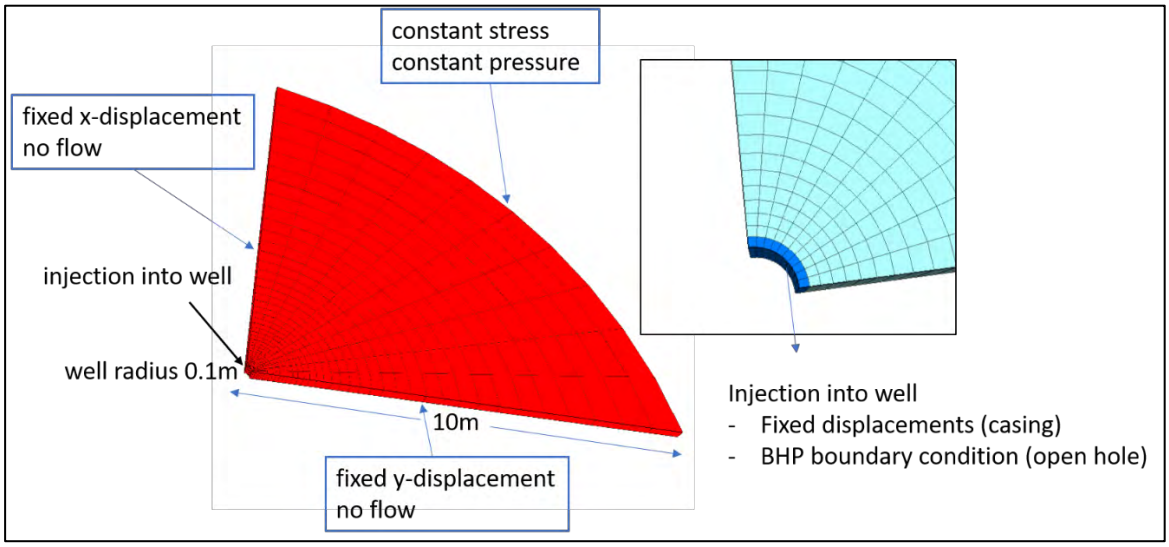

Figure C3. Geometry of the THCM model for acid injection

3 Model results of soft-chemical stimulation

3.1 Field-scale geothermal reservoir reactive transport model (RTM)

Reactive transport modelling was performed to investigate the effect of acid stimulation by HCl and soft stimulation by CO_2 by comparing these simulations with a base case model for conventional geothermal operations. CO_2 dissolved soft-stimulating scenarios were defined (table C4), to study the effect of injecting various CO_2 concentrations, in addition to the natural CO_2 in the formation water, on reservoir flow performance compared to acid stimulation. For the comparison, basecase flow is performed after acid stimulation. The geothermal fluid is based on a Delft formation water originally containing dissolved gases in the reservoir (mainly methane (CH_4) and CO_2), related to hydrocarbon charging of the region. The base case simulation assumes that the geothermal fluid is injected as it was produced, without chemical changes (no outgassing) only cooling. The first soft-stimulation scenario assumes outgassing of all CH_4 and CO_2 at the surface, burning of the produced CH_4, capturing all released CO_2 and co-injecting this amount dissolved in the geothermal water. This case would prevent emissions of greenhouse gasses related to outgassing, representing carbon-neutral geothermal energy production. For the second scenario, CO_2 is dissolved into the injected water up to brine saturation level using an external source of CO_2. This would maximize CO_2 emission reduction and even contribute to CO_2 storage. The scenarios all have different masses of dissolved CO_2 injection (table C4). Dissolving different levels of CO_2 affects the chemistry of the injected waters. To include this effect, the water compositions are initialized with the various amounts of CO_2 in proportion to the injection rates (table C4).

Table C4: Base case injection and two soft-stimulation scenarios with dissolved CO_2.

Scenario	CO_2 injection rate (kg/s)	Dissolved CO_2, HCO_3^- (mol/l)
1. Base case	0.042	2.48E-02
2. CH_4-use and CO_2 re-injection	0.098	5.36E-02
3. CO_2 dissolved	1.834	5.57E-01

3.1.1 Basecase flow results without stimulation

After 30 years of injection, a cold water plume has formed around the injection well as a result of the conventional geothermal operations (Figure C5). The production and re-injection of the geothermal water caused a pressure gradient between the higher pressure injection well on the left and a lower pressure production well (Figure C6). Due to the cold water injection and cooling of the reservoir, the carbonates start to dissolve near well (Figure C7). Calcites dissolves faster, followed by siderite dissolution. Other chemical reactions are minor and include precipitation of barite, kaolinite and smectite (results not shown). These minerals form due to their decreasing solubility with decreasing temperatures. With the currently used formation water, the model results show limited adverse chemical reactions due to cooling that could clog the pore space. Carbonate dissolution has a clear impact on the flow properties of the reservoir. The porosity increases from 18% to 28% in the near-well area, with a related permeability increase (Figure C8).

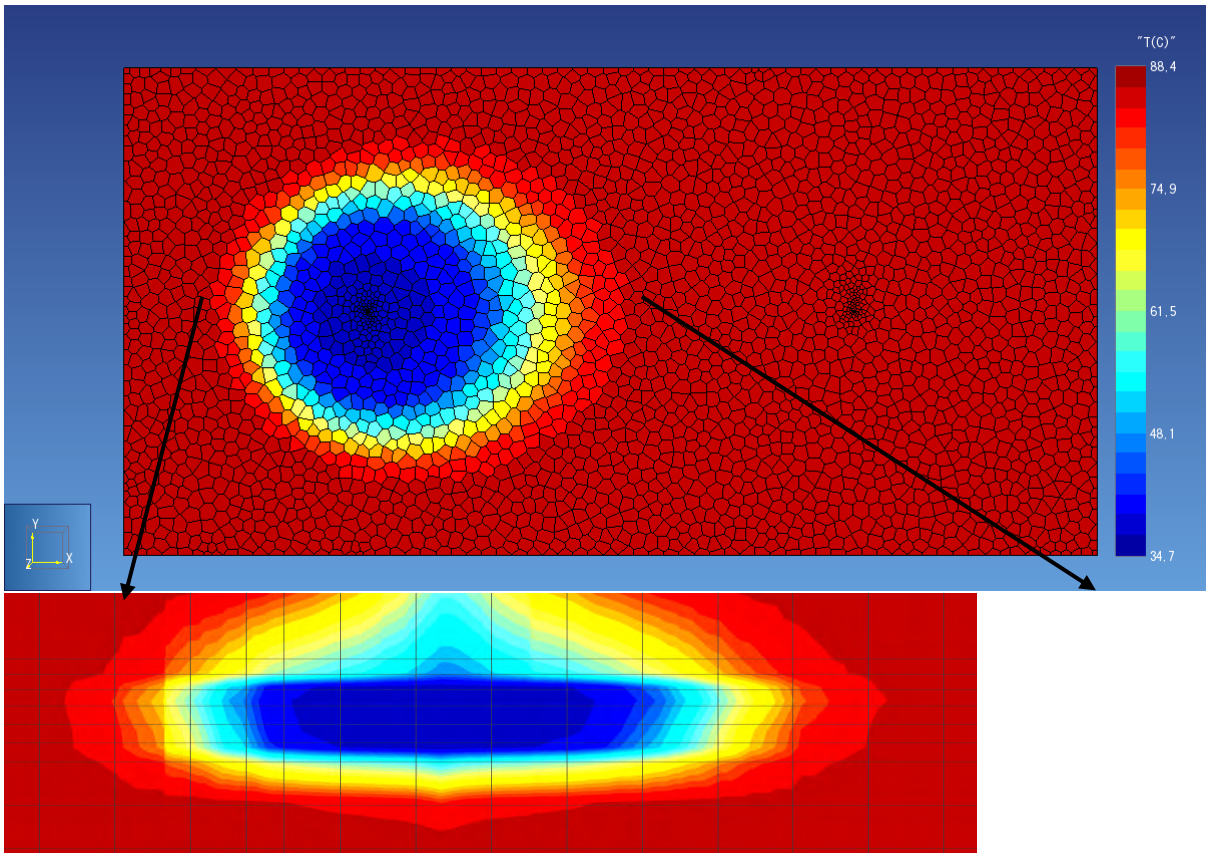

Figure C5. Aerial view (top) and vertical cross-section (bottom) of the model (3 km wide) around the injection well (1 km wide) illustrating the cold water plume around the injection well.

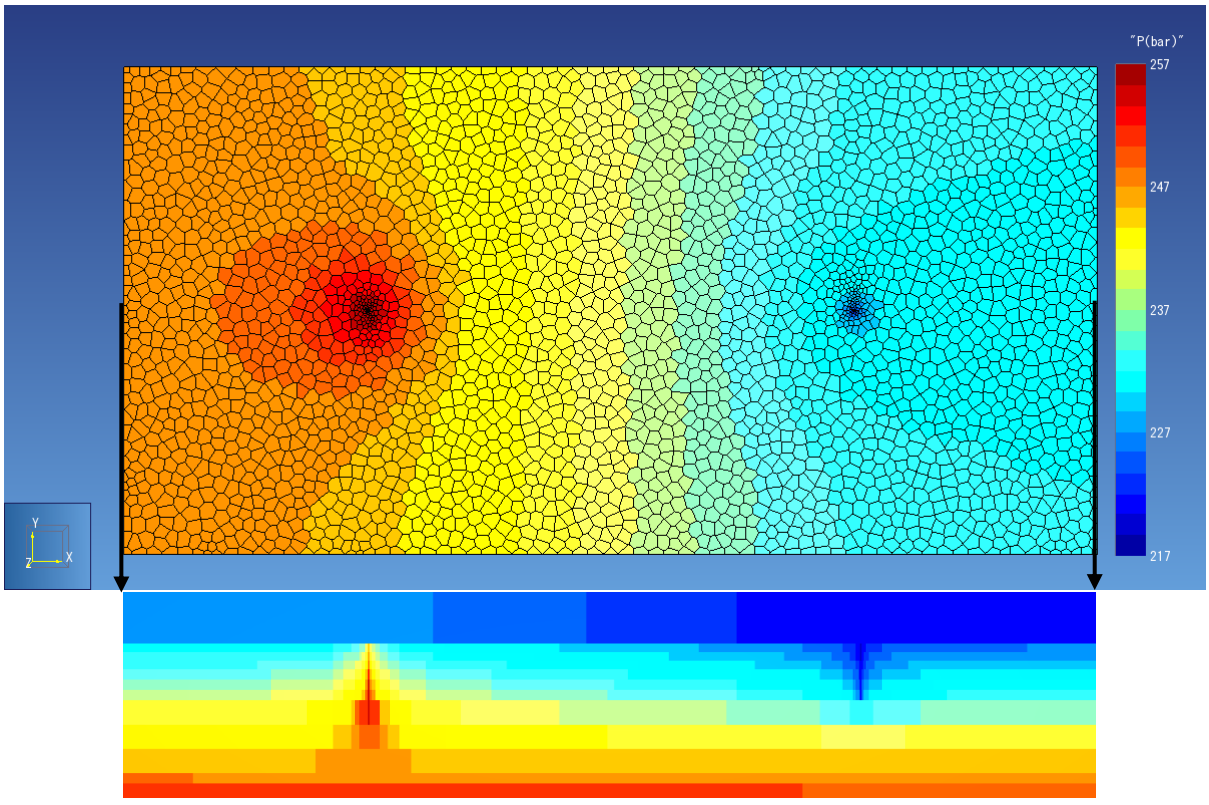

Figure C6. Aerial view and cross-section of the model (3 km wide), illustrating the higher pressure around the injection well and decreased pressure around the production well.

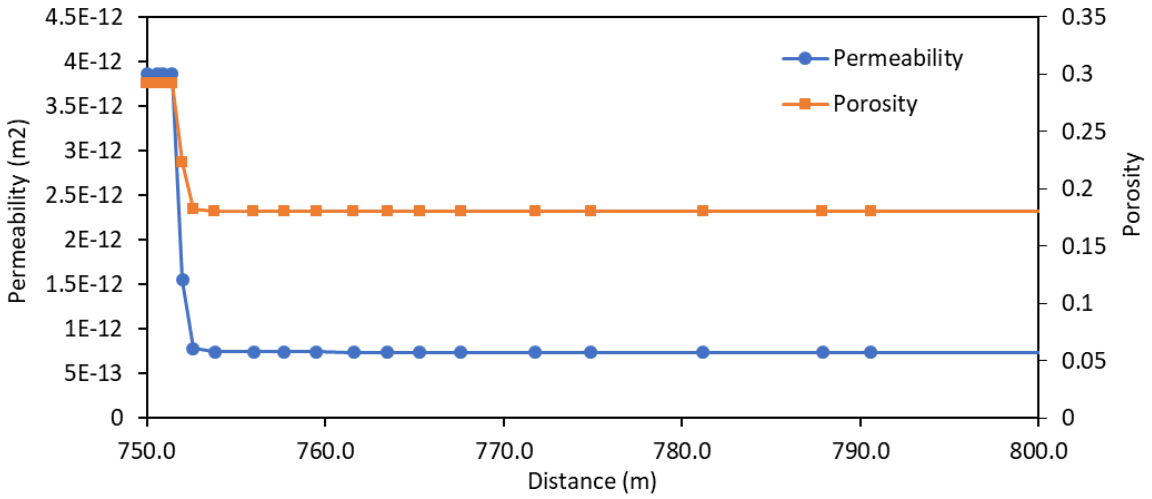

Figure C7. Porosity and permeability development with distance from the injection cell at 750m.

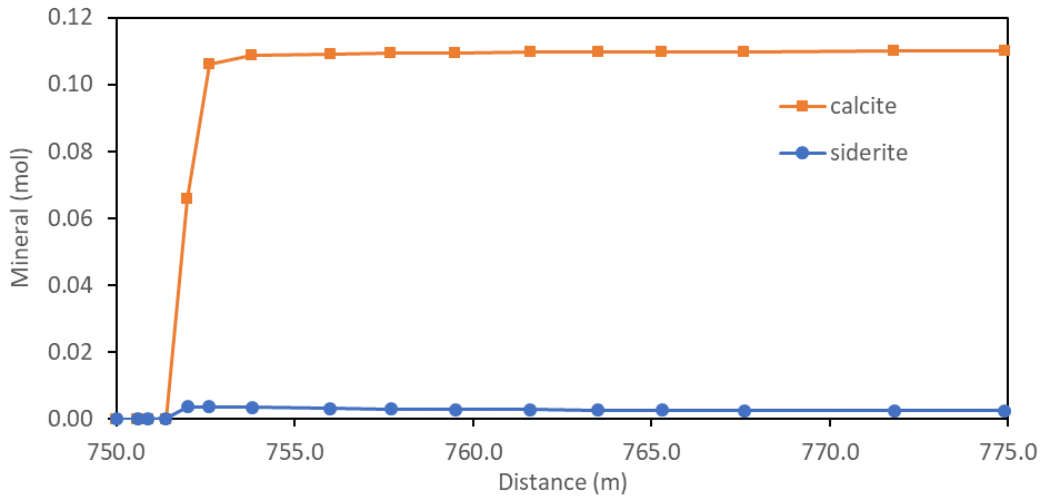

Figure C8. Calcite and siderite volume fraction with distance from the injection cell at 750m.

3.1.2 Chemical treatment scenarios

As a first assessment of the carbonate-dissolution potential, the model is run with continuous acid injection (with the same rate as geothermal injection) and compared to the different CO_2 dissolved scenarios. Carbonate dissolution defines the stimulation potential since the decrease in carbonate volume fraction is directly related to the increase in pore volume.

After 8 hours of acid injection, all calcite is dissolved in the first cell around the wellbore (Figure C9). Siderite dissolution takes approximately ten times as long (Figure C10). The base case injection contains no additional CO_2 but it also has a carbonate dissolution potential since the low temperature increases carbonate solubility. Carbonate dissolution is the slowest for the base case with ~10000 hours to dissolve all calcite (Figure C9). When injecting all produced CO_2 in the geothermal water (outgassed and derived from burning outgassed CH_4), it takes 5330 hours (0.6 years) to dissolve all calcite near-well. The scenario with CO_2 up to brine solubility requires only 955 hours (40 days) to dissolve all calcite. The same trend in dissolution potential of the different scenarios is observed for siderite, with its dissolution is always slower than for calcite (Figure C9 and C10).

To compare the effect of acid stimulation on geothermal performance, an acid job is simulated for 8 hours to achieve full calcite dissolution around the well. After acid stimulation, base case geothermal production and injection is simulated for 4 years (Figure C11). Figure C11 shows no shows no significant difference between base case injection with and without an initial acid job. These model results indicate that although acid stimulation achieves much faster carbonate dissolution, in the long run injection of cooled water can yield the same effect.

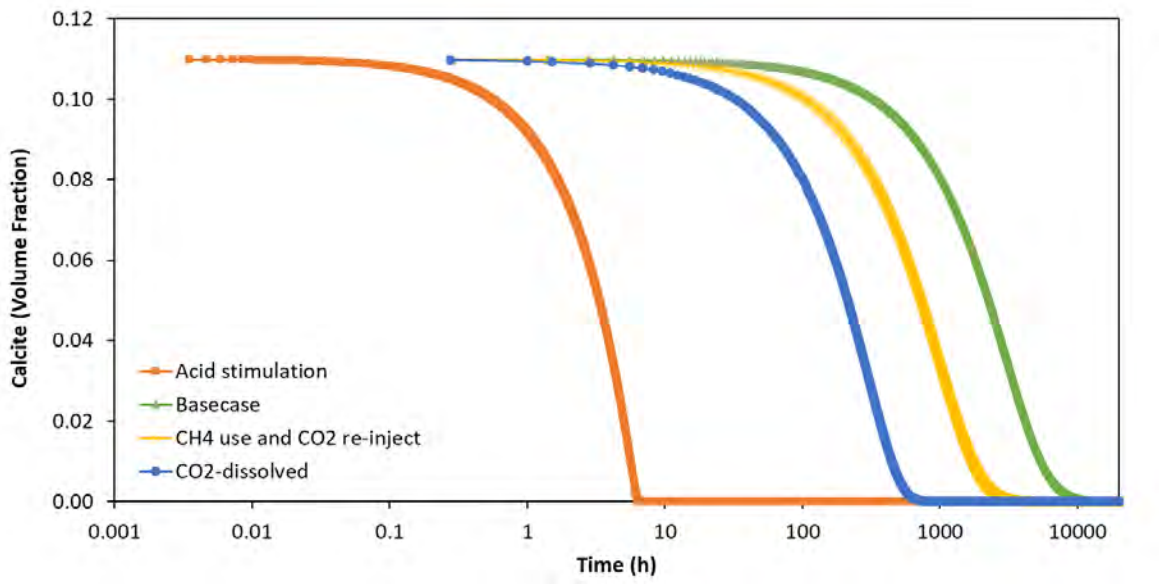

Figure C9. Calcite content in the injection cell over time (logarithmic scale) for scenarios of acid injection and different dissolved CO_2 content.

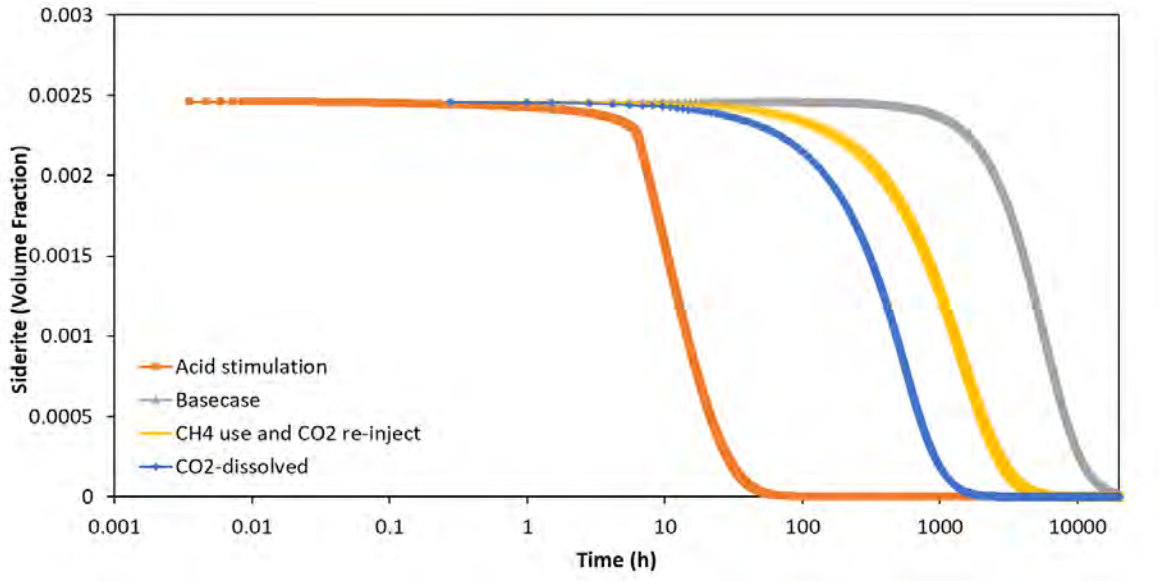

Figure C10. Siderite content in the injection cell over time (logarithmic scale) for scenarios of acid injection and different dissolved CO_2 content.

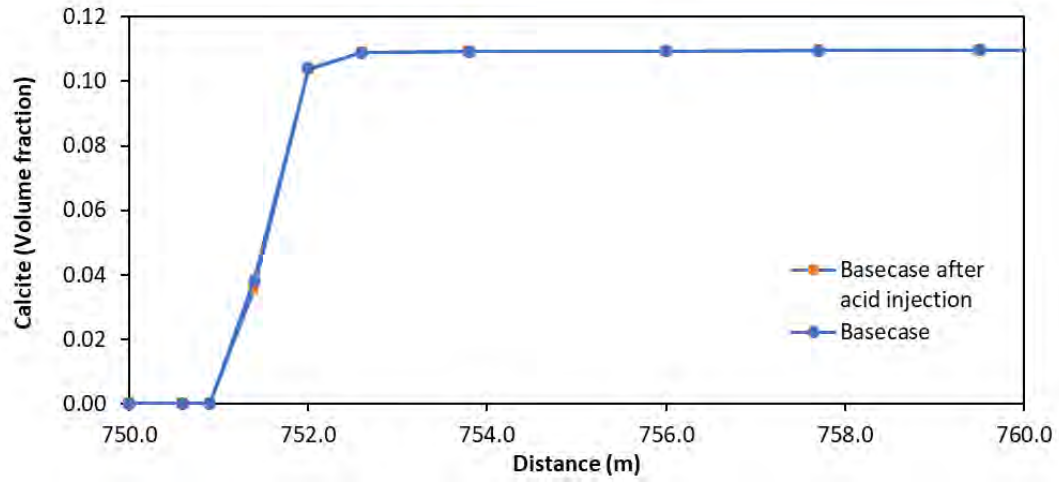

Figure C11. Calcite content with distance from the injection well after 4 years of operations for base case injection with and without an acid job before geothermal operation.

The pressure development is of a geothermal reservoir is important since the required injection pressure affects the operational costs. The pressure can be related to the flow rate to define the productivity/injectivity index. The current reservoir model uses a fixed flow rate, so the pressure development can be used as an indication of reservoir performance. The different CO_2 scenarios result in different a different mass of the injected geothermal fluid. Cooling the geothermal fluid increases its density and viscosity, but the density effect greatly outweighs the negative effect of the increased viscosity (Veldkamp et al. 2016). Both the changed mass and density control the pressure development in the reservoir. Furthermore, chemical reactions and related change of the pore volume will change the reservoir pressure with a fixed injection rate. The model is used to assess the effect of all processes combined on the reservoir performance.

The base case results in the lowest pressure (Figure C11). When an acid job is simulated before base case injection and production, the pressure is not significantly different on the long term (after 7 years). These results again indicate that the faster effect of acid stimulation can be accomplished with long-term injection of cooled water. Injecting CO_2 saturated brine shows a significant pressure increase due to the added mass of CO_2. The pressure increase is 20 bar above the initial value of 255 bar (figure C11). However, the pressure development in a specific reservoir and hence the effect of a chemical treatment will depend on the mineralogy (carbonate content) of the reservoir, the amount of CO_2 added and also largely of the size of the reservoir.

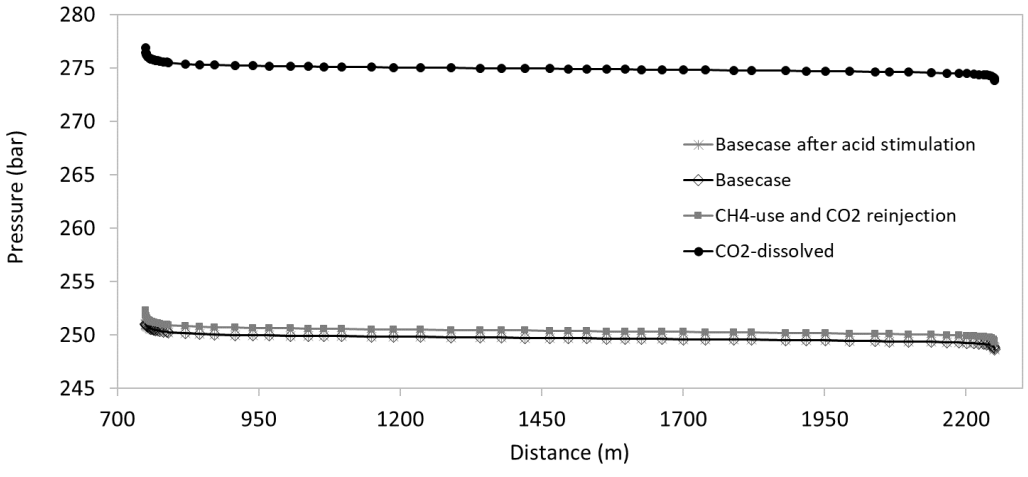

Figure C11. Pressure development after 7 years of geothermal production for the different scenarios for a cross section of the model at y= 750 meter, in the middle of the reservoir at z= -2425 m.

3.2 Results radial THMC model

The model can be used to assess the coupled effects of the pressure and temperature development, mineral dissolution and mechanics on porosity and permeability evolution, the potential mechanical degradation of strength and associated compaction and the potential of thermal fracturing near the injection well. As noted before, at this stage the software has been used for trial runs, as more input is needed on the specific relation between e.g. changes in the chemical composition and porosity of sandstone rocks and mechanical properties such as compaction coefficient and strength. Future experimental studies should provide insight and data on the relation between the dissolution of cement, porosity changes and the mechanical strength of rock samples, which can then serve as input to the coupled THCM models. In Figure C4 some preliminary examples of model outcomes of the THCM model are shown.

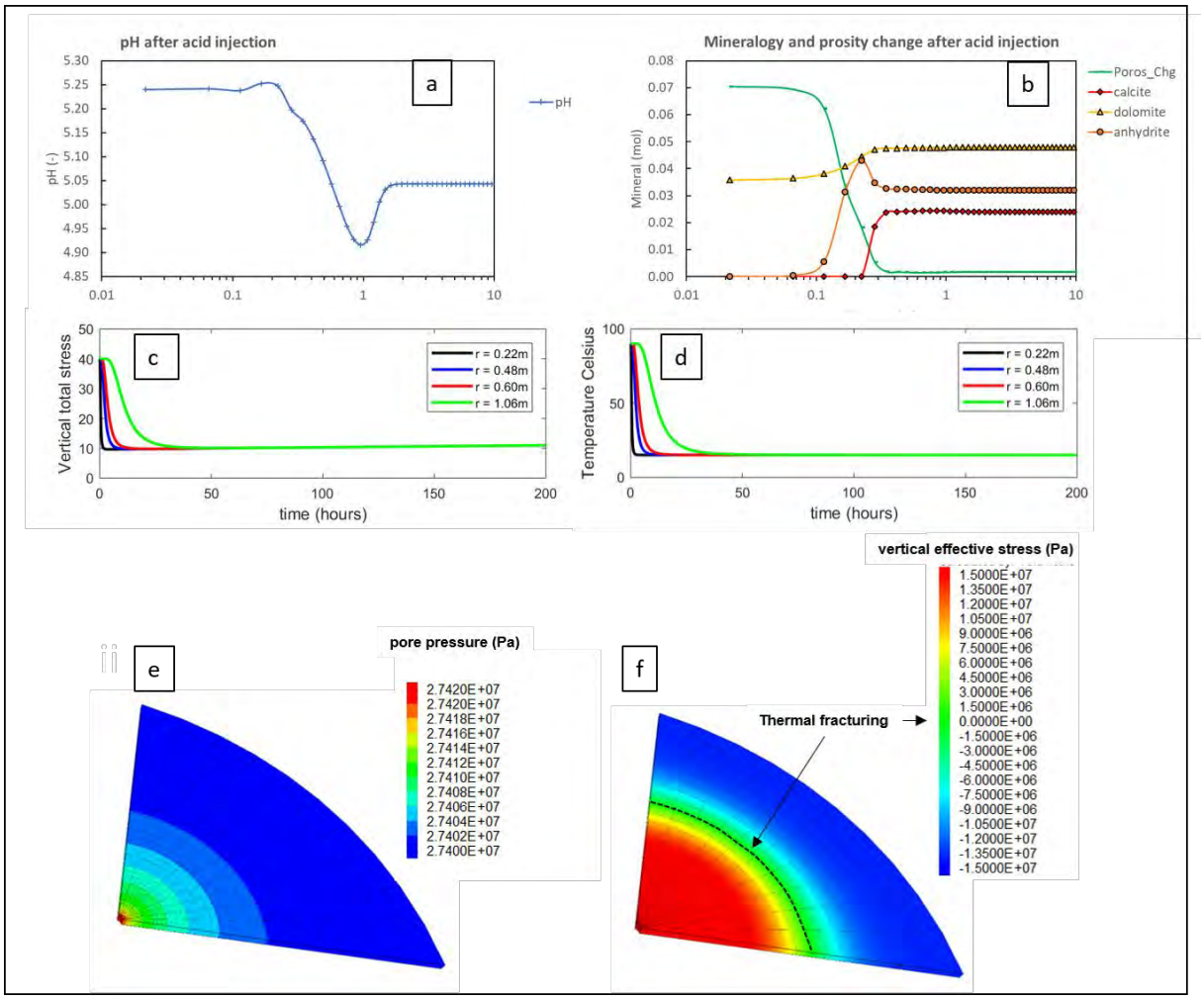

Figure C4. Example of model results for the THCM model with a) Evolution of pH after acid injection, b) mineralogy and porosity change after injection, c) evolution of vertical total stress during injection, d) temperature evolution during injection, e) pore pressure at the end of injection, f) total vertical stress and potential for thermal fracturing after injection.

Discussion and conclusions

The chemical processes during acid stimulation and CO_2 soft-stimulation and the effects on the flow in a geothermal reservoir are assessed with reactive transport simulations using TOUGHREACT software. Dissolution of carbonates in the reservoir rock results in an increased injectivity and hence enhanced geothermal performance.

Acid stimulation with HCl is effective in dissolving carbonate (cement) in sandstones. The dissolution potential of cold water can achieve the same results in good quality reservoir studied, but low permeability reservoirs may require the faster results of an acid stimulation. Carbonate dissolution similar to an acid job can be achieved within years of normal geothermal operation in a functional reservoir. When the geothermal fluid is CO_2 enriched, the soft-stimulation potential of the geothermal fluid is even larger and results in an increased area of carbonate dissolution around the wellbore. With the selected mineralogy, the porosity is dominantly controlled by calcite dissolution which yields a maximum porosity increase from 18 to 29 % and a permeability improvement from 750 mD to 3.75 D. Soft stimulation with dissolved CO_2 has the additional benefit of reducing CO_2 emissions into the atmosphere.

Different factors add up to the pressure response of the reservoir and hence the possible flow rates and geothermal performance. Both cooling (density increase) and dissolution (pore space increase) decrease the reservoir pressure. CO_2 addition increases the reservoir pressure because of the added mass but can decrease the pressure by inducing dissolution and porosity increase. The final result depends on the carbonate content of the reservoir and the amount of CO_2 added. Detailed reactive transport models are required to assess the effect of performance enhancement by chemical-soft-stimulation. The THMC models can be used to assess the coupled effects of the pressure and temperature development, mineral dissolution and mechanics on porosity and permeability evolution, the potential mechanical degradation of strength and associated compaction and the potential of thermal fracturing near the injection well. Future experimental studies should provide insight and data on the relation between the dissolution of cement, porosity changes and the mechanical strength of rock samples, which can then serve as input to the coupled THCM models.

REFERENCES

1. Ali S.A., Kalfayan L., and Montgomery C., Acid stimulation, SPE Monograph Series, Vol. 26, 305 pp, 2016.
2. Alt-Epping, P., Waber, H., Diamond, L., and Eichinger, L.: Reactive transport modeling of the geothermal system at Bad Blumau, Austria: Implications of the combined extraction of heat and CO_2, Geothermics, 45, (2013), 18-30.
3. Blanc Ph., Lassin A., Piantone P., Azaroual M., Jacquement N., Fabbri A., Gaucher, E.C., (2012) Thermoddem: A geochemical database focused on low temperature water/rock interactions and waste materials, Applied Geochemistry, 27, 2107-2116.
4. Boch, R., Leis, A., Haslinger, E., Goldbrunner, J. E., Mittermayr, F., Fröschl, H., and Dietzel, M.: Scale-fragment formation impairing geothermal energy production: interacting H_2S corrosion and $CaCO_3$ crystal growth, Geothermal Energy, 5(1), (2017), art. no. 4.
5. Hommel, J., Coltman, E., Class, H.: Porosity–Permeability Relations for Evolving Pore Space: A Review with a Focus on (Bio)geochemically Altered Porous Media, Transport in Porous Media, 124 (2), (2018), 589-629.
6. Huq, F., Haderlein, S. B., Cirpka, O. A., Nowak, M., Blum, P., and Grathwohl, P.: Flow-through experiments on water–rock interactions in a sandstone caused by CO_2 injection at pressures and temperatures mimicking reservoir conditions, Applied Geochemistry, 58, (2015), 136-146.

7. Lasaga, A.C.; Soler, J.M.; Ganor, J.; Burch, T.E. and Nagy, K.L., Chemical weathering rate laws and global geochemical cycles. Geochim. Cosmochim. Acta 1994; 58(10), 2361-2386.
8. Palandri, J.L., Kharaka, Y.K.: A compilation of rate parameters of water-mineral interaction kinetics for application to geochemical modeling. U.S. Geological Survey, Open File Report 2004-1068.
9. Portier, S., L. André, and F.-D. Vuataz, Review on chemical stimulation techniques in oil industry and applications to geothermal systems. Engine, work package, 2007. 4: p. 32
10. Pruess, K. ECO2N : A TOUGH2 Fluid Property Module for Mixtures of Water, NaCl, and CO_2; Lawrence Berkeley National Laboratory: Berkeley, CA, USA, 2005.
11. Pruess, K., Oldenburg, C. and Moridis, G.: TOUGH2 User's Guide, Version 2.0. Report LBNL-43134. Lawrence Berkeley National Laboratory, Berkeley, CA (1999).
12. Rae, P., & Di Lullo, G. (2003, January 1). Matrix Acid Stimulation - A Review of the State-Of-The-Art. Society of Petroleum Engineers. doi:10.2118/82260-MS
13. Taron, J., & Elsworth, D. (2010). Coupled mechanical and chemical processes in engineered geothermal reservoirs with dynamic permeability. International Journal of Rock Mechanics and Mining Sciences, 47(8), 1339-1348. https://doi.org/10.1016/j.ijrmms.2010.08.021
14. Ungemach, P.: Reinjection of cooled geothermal brines into sandstone reservoirs, Geothermics, 32(4-6), (2003), 743-761.
15. Verma, A., Pruess, K.: Thermohydrological conditions and silica redistribution near high-level nuclear wastes emplaced in saturated geological formations, Journal of Geophysical Research, 93 (B2), (1988), 1159-1173.
16. Veldkamp, J.G., Loeve, D., Peters, E., Nair, R., Pizzocolo, F., and Wilschut, F.: Thermal fracturing due to low injection temperatures in geothermal doublets. (2016).
17. Wasch, L.J.: Geothermal Energy-Scaling potential with cooling and CO_2 degassing. TNO report. TNO 2013 R11661. (2014).
18. Wasch, L.J., Dijkstra, H.E. and Koenen, M.K., Soft-stimulating Injection Procedures to Improve Geothermal Reservoir Performance - Proceedings, World Geothermal Congress, 2020 Reykjavik.
19. Xu T., Sonnenthal E., Spycher N., Zheng L., (2014) TOUGHREACT V3.0-OMP Reference manual: A parallel simulation program for non-isothermal multiphase geochemical reactive transport. LBNL765 Draft.
20. Xu, T.; Sonnenthal, E.; Spycher, N.; Pruess, K. TOUGHREACT—A simulation program for non-isothermal multiphase reactive geochemical transport in variably saturated geologic media: Applications to geothermal injectivity and CO2 geological sequestration. Computat. Geosci. 2006, 32, 145–165.

Imprint

Project Lead	GFZ German Research Centre for Geosciences Telegrafenberg 14473 Potsdam (Germany) www.gfz-potsdam.de/en/home/
Project Coordinator	Prof. Ernst Huenges huenges@gfz-potsdam.de +49 (0)331/288-1440
Project Manager	Dr. Justyna Ellis ellis@gfz-potsdam.de +49 (0)331/288-1526
Project Website	www.destress-H2020.eu

Liability claim

DESTRESS is co-funded by

National Research Foundation of Korea (NRF)

Korea Institute for Advancement of Technology (KIAT)

Swiss State Secretariat for Education, Research and Innovation (SERI)